The JWST-NIRCam View of Sagittarius C. II. Evidence for Magnetically Dominated H ii Regions in the Central Molecular Zone

(article starts on next page)

The JWST-NIRCam View of Sagittarius C. II. Evidence for Magnetically Dominated H II Regions in the Central Molecular Zone

John Bally[1] , Samuel Crowe[2] , Rubén Fedriani[3] , Adam Ginsburg[4] , Rainer Schödel[3] , Morten Andersen[5] , Jonathan C. Tan[2,6] , Zhi-Yun Li[2] , Francisco Nogueras-Lara[5] , Yu Cheng[7] , Chi-Yan Law[8] , Q. Daniel Wang[9] , Yichen Zhang[2,10] , and Suinan Zhang[11]

[1] Center for Astrophysics and Space Astronomy, Department of Astrophysical and Planetary Sciences University of Colorado, Boulder, CO 80389, USA; john.bally@colorado.edu
[2] Dept. of Astronomy, University of Virginia, Charlottesville, VA 22904, USA
[3] Instituto de Astrofísica de Andalucía, CSIC, Glorieta de la Astronomía s/n, E-18008 Granada, Spain
[4] Department of Astronomy, University of Florida, P.O. Box 112055, Gainesville, FL, USA
[5] European Southern Observatory, Karl-Schwarzschild-Strasse 2, D-85748 Garching bei München, Germany
[6] Department of Space, Earth & Environment, Chalmers University of Technology, 412 93 Gothenburg, Sweden
[7] National Astronomical Observatory of Japan, 2-21-1 Osawa, Mitaka, Tokyo 181-8588, Japan
[8] Osservatorio Astrofisico di Arcetri, Largo Enrico Fermi, 5, 50125 Firenze FI, Italy
[9] Department of Astronomy, University of Massachusetts, Amherst, MA 01003, USA
[10] Department of Astronomy, Shanghai Jiao Tong University, 800 Dongchuan Road, Minhang, Shanghai 200240, People's Republic of China
[11] Shanghai Astronomical Observatory, Chinese Academy of Sciences, 80 Nandan Road, Shanghai 200030, People's Republic of China

Abstract

We present JWST-NIRCam narrowband, 4.05 μm Br α images of the Sgr C H II region, located in the central molecular zone (CMZ) of the Galaxy. Unlike any H II region in the solar vicinity, the Sgr C plasma is dominated by filamentary structure in both Br α and the radio continuum. Some bright filaments, which form a fractured arc with a radius of about 1.85 pc centered on the Sgr C star-forming molecular clump, likely trace ionization fronts. The brightest filaments form a "π-shaped" structure in the center of the H II region. Fainter filaments radiate away from the surface of the Sgr C molecular cloud. The filaments are emitting optically thin free–free emission, as revealed by spectral index measurements from 1.28 GHz (MeerKAT) to 97 GHz (Atacama Large Millimeter/ submillimeter Array). But, the negative in-band 1 to 2 GHz spectral index in the MeerKAT data alone reveals the presence of a nonthermal component across the entire Sgr C H II region. We argue that the plasma flow in Sgr C is controlled by magnetic fields, which confine the plasma to ropelike filaments or sheets. This results in the measured nonthermal component of low-frequency radio emission plasma, as well as a plasma β (thermal pressure divided by magnetic pressure) below 1, even in the densest regions. We speculate that all mature H II regions in the CMZ, and galactic nuclei in general, evolve in a magnetically dominated, low plasma β regime.

Unified Astronomy Thesaurus concepts: Emission nebulae (461)

1. Introduction

The central molecular zone (CMZ) surrounding the Galactic center (GC) of our Milky Way is a region characterized by extreme conditions. The densities, temperatures, pressures, turbulent motions, and magnetic field strengths in CMZ molecular clouds are orders of magnitude larger than in the Galactic disk (see, e.g., J. Bally et al. 1987, 1988; U. Giveon et al. 2002; K. Ferrière 2009; J. M. D. Kruijssen et al. 2014; A. Ginsburg et al. 2016). However, the current star formation rate in the CMZ ($\sim 0.08\ M_\odot\ \mathrm{yr}^{-1}$; J. D. Henshaw et al. 2023) is around an order of magnitude lower than expected from its 2 to $5 \times 10^7\ M_\odot$ reservoir of dense molecular gas (K. Ferrière et al. 2007). Three quarters of the molecular gas is at positive galactic longitudes and radial velocities; most of the compact 24 μm sources are at negative galactic longitudes (J. Bally et al. 1988; F. Yusef-Zadeh et al. 2009). M. C. Sormani et al. (2018) have theoretically explained this asymmetry as the result of unsteady flow of gas in a barred potential.

The CMZ is strongly magnetized (K. Ferrière 2009; R. M. Crocker et al. 2010; S. Nishiyama et al. 2010; A. Mangilli et al. 2019; N. O. Butterfield et al. 2024a, 2024b; D. Paré et al. 2024). Polarized radio continuum emission from hundreds of nonthermal filaments (NTFs) in the CMZ trace relativistic, magnetically confined synchrotron emission regions (F. Yusef-Zadeh et al. 1984, 2022a, 2022c, 2022b, 2023). High-resolution radio observations at 1.28 GHz with MeerKAT (I. Heywood et al. 2022) demonstrate that filaments pervade the CMZ at a wide range of length scales, from less than 1 pc to over 100 pc. Most NTFs trace either magnetic ropes or edge-on sheets oriented roughly orthogonal to the Galactic plane, thus tracing a poloidal component of the field. Many NTFs are associated with CMZ star-forming regions containing populations of O-type and Wolf–Rayet (WR) stars (F. Yusef-Zadeh 2003). Dust polarization measurements show that the CMZ molecular clouds are threaded by magnetic fields that, on large scales, tend to be roughly parallel to the Galactic plane, thus tracing a toroidal component of the field (S. Nishiyama et al. 2010; A. Mangilli et al. 2019; Y. Guan et al. 2021; Y. Hu et al. 2022). Equipartition arguments applied to the NTFs imply field strengths of about 0.1 to 0.4 mG in the intercloud medium of the CMZ (R. M. Crocker et al. 2010; F. Yusef-Zadeh et al. 2022d). The S. Chandrasekhar & E. Fermi (1953) method

applied to the dust polarization data from CMZ clouds implies 0.1 to 10 mG fields (T. Pillai et al. 2015; X. Pan et al. 2024). K. Ferrière (2009) used the apparent resistance of the NTFs to bending by collisions with CMZ molecular clouds to derive field strengths of order 0.1 to 10 mG. R. G. Tress et al. (2024) present numerical simulations of the inner Galaxy and show that strong magnetic fields are essential for driving mass inflow from the outer Galaxy onto the CMZ along the leading-edge dust lanes of the Milky Way's stellar bar.

Sagittarius C (hereafter Sgr C) is the most luminous star-forming region in the negative galactic longitude portion of CMZ (S. Kendrew et al. 2013). Assuming Sgr C is at the same distance as Sgr A*, we adopt a galactocentric distance of 8.15 ± 0.15 kpc to the region (M. J. Reid et al. 2019). Sgr C has a luminosity $L \sim 10^6 L_\odot$ and is associated with a prominent H II region detected from mid-infrared to radio wavelengths (H. S. Liszt & R. W. Spiker 1995; C. C. Lang et al. 2010; M. J. Hankins et al. 2020). F. Nogueras-Lara (2024) found evidence for $>10^5 M_\odot$ of young stars around Sgr C, with ages of up to ~20 Myr, mixed with a larger, older population with ages over 2 Gyr. J. S. Clark et al. (2021) classified two bright infrared sources (Two Micron All Sky Survey, 2MASS, J17443734-2927557 and J17444083-2926550) as WR stars within the Sgr C H II region using spectroscopy, implying that the OB star population in the Sgr C H II region has an age of at least ⩾3Myr. Furthermore, Sgr C has been suggested to be a connection point to a stream of gas and dust linking the CMZ and nuclear stellar disk to the Galactic bar (S. Molinari et al. 2011; J. D. Henshaw et al. 2023), motivating the strong 24 μm emission in this region (S. J. Carey et al. 2009) as high amounts of warm dust heated by ionizing stars. This also explains the large gas reserves in this region that are necessary to produce its observed star formation activity (S. Kendrew et al. 2013; X. Lu et al. 2020, 2021; S. Crowe et al. 2025, hereafter Paper I).

Observations using the Infrared Spectrograph (IRS) on the Spitzer Space Observatory combined with X-rays and models using the CLOUDY and Starburst99 computer codes indicates that the Sgr C H II region has an age of ~4 Myr, an electron density $n_e \simeq 300$ cm^{-3} (which compares reasonably well to the electron density $n_e \simeq 200$ cm^{-3} derived previously by H. S. Liszt & R. W. Spiker 1995), and a Lyman photon luminosity of $Q_0 \simeq 1 \times 10^{50}$s^{-1} (J. P. Simpson 2018). A giant molecular cloud (GMC) adjacent to the H II region hosts ongoing massive star formation (S. Kendrew et al. 2013; X. Lu et al. 2019). X. Lu et al. (2024) and D. Paré et al. (2024) show that the cloud has a prominent cometary, head–tail morphology and that the magnetic field orientations follow the cloud edges. However, the dust polarization measurements tend to probe deeper into the cloud rather than the cloud surface. Nevertheless, the cometary shape and tendency of the field to wrap around the cloud seem to imply an interaction between the adjacent H II region and the cloud. A similar field morphology is seen in the Messier 16 "Pillars of Creation" (K. Pattle et al. 2018). Luminous, massive protostars are found close to the interface between the Sgr C cloud and the Sgr C H II region (S. Kendrew et al. 2013; X. Lu et al. 2020; Paper I), which indicates either that compressive pressures from the H II region have triggered star formation or that photoablation has uncovered the star-forming region.

We present JWST-NIRCam observations of the Sgr C H II region that reveal a uniquely filamentary morphology in the mid-infrared Brackett-α (Br α) hydrogen recombination line. The filamentary structure is also seen in the 3 mm (97 GHz) and 23 cm (1.28 GHz) wavelength radio continuum. Inspection of the MeerKAT 1.28 GHz image shows that filamentary morphology is not unique to Sgr C; it is found in all mature CMZ H II regions, most notably Sgr B1. None of the foreground H II regions located in the Galactic disk imaged by MeerKAT exhibit such filamentation, nor is such a morphology seen in other H II regions in the Galactic disk, such as the Orion Nebula (C. R. O'Dell 2001). In the Galactic disk, thermal pressure dominates magnetic pressure in the evolution of H II regions (based on typical Galactic disk field strengths; R. M. Crutcher 2012). We argue that, in the CMZ, the filamentary structure of H II regions indicates that magnetic pressure is larger than thermal pressure during most of a mature H II region's evolution. We present a simple, intuitive description of the expected evolution of magnetically dominated H II regions.

2. Observations

2.1. James Webb Space Telescope

A single pointing of JWST-NIRCam imaging data was taken of the Sgr C region on the 2023 September 22 (program ID: 4147, PI: S. Crowe). The filter set included eight medium- and narrowband filters from ~1–5 μm; most relevant to this work is F405N, which traces the Br α hydrogen recombination line at 4.05 μm and the two adjacent medium-band filters, F360M and F480M. The images taken through the F405N filter were continuum subtracted by linearly interpolating the stellar fluxes in the medium-band F360M and F480M filters to estimate the mean continuum flux at 4.05 μm. For further details on the filter set, observational setup, data reduction, and continuum-subtraction of the Sgr C NIRCam data, we defer to Paper I. The final composite image has a field of view (FOV) of $2'.39 \times 5'.91$ (5.67 × 14.01 pc). The long dimension of the image is oriented nearly north–south at a position angle (V3PA) of $1°.39$ in equatorial coordinates and $59°.94$ in Galactic coordinates, causing the pixels to be at an angle with respect to both celestial and Galactic coordinates.

2.2. Ancillary Millimeter and Radio Data

We use Atacama Large Millimeter/submillimeter Array (ALMA) continuum and spectral line data obtained as part of the ALMA CMZ Exploration Survey (ACES). Comprehensive details on the ACES survey and data reduction are presented in A. Ginsburg et al. (2025, in preparation) and D. L. Walker et al. (2025, in preparation). In the analysis presented here, we use the 3 mm line-free continuum image formed from four passbands used by ACES. The central frequencies and bandwidths of the four passbands used to form these images are [$\nu = 86.2$ GHz, $\Delta\nu = 0.46$ GHz], [$\nu = 86.9$ GHz, $\Delta\nu = 0.46$ GHz], [$\nu = 98.6$ GHz, $\Delta\nu = 1.875$ GHz], and [$\nu = 100.5$ GHz, $\Delta\nu = 1.875$ GHz]. For a flat-spectrum source, the effective central frequency, weighted by the passbands, is 97 GHz. We use only the 12 m ALMA data from ACES, which means that structure on angular scales larger than about 30″ is resolved out, while fluxes of features having structure on angular scales smaller than 30″ are preserved. The effective beam size of the ALMA images is $1''.97 \times 1''.52$. In addition to the continuum images, we use the ACES data cube featuring the HNCO (4–3) line at 87.925238 GHz.
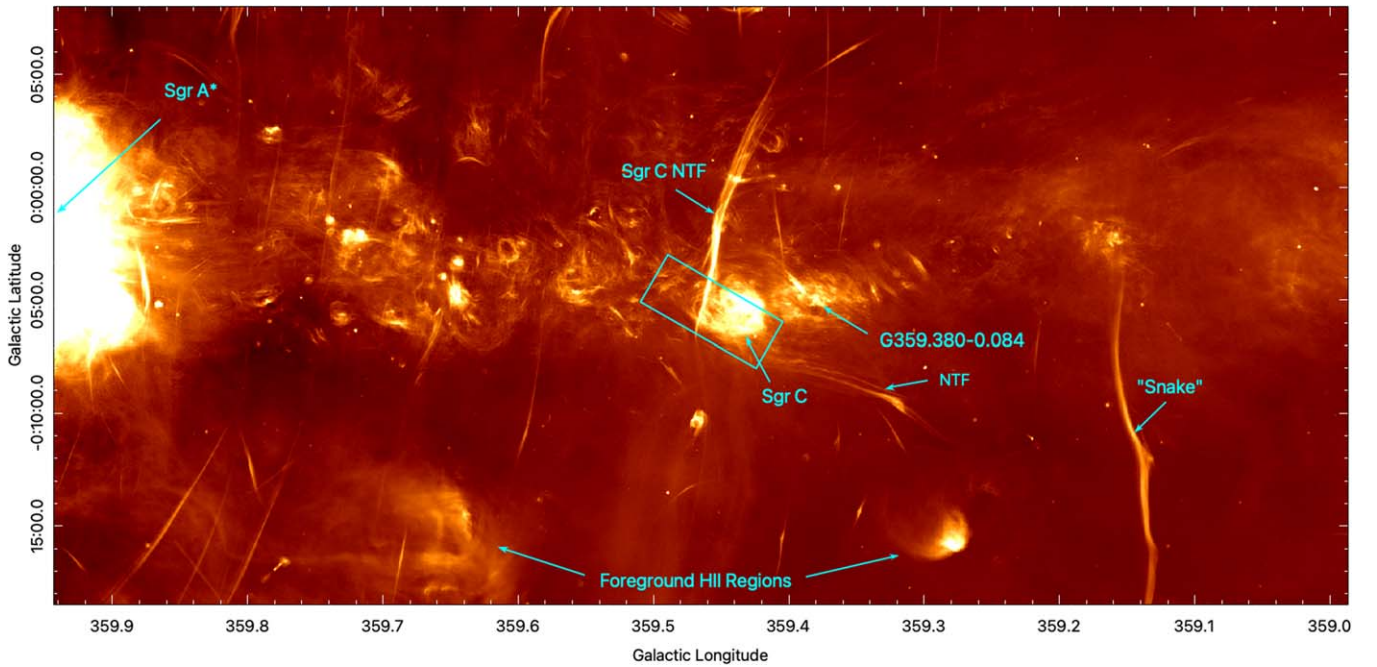
Figure 1. The JWST field (cyan rectangle) shown on a MeerKAT radio continuum image centered at 1.28 GHz (I. Heywood et al. 2022). While most NTFs, such as the Sgr C NTF, run orthogonal to Galactic plane, the NTF located to the lower right of Sgr C is nearly parallel to the Galactic plane, as mentioned in the text.

We use the total intensity map at 1.28 GHz from the MeerKAT telescope presented in I. Heywood et al. (2022) and publicly available in the MeerKAT archive. This survey includes broad coverage of the entire CMZ region, including higher- and lower-galactic latitudes than the ACES survey. We also use the MeerKAT spectral index map presented in I. Heywood et al. (2022), which covers the same regions as the total intensity map. The spectral index α is defined by

$$F_\nu = C\nu^\alpha \qquad (1)$$

where F is the flux at a given frequency ν, and C is a generic constant of proportionality. Therefore, the spectral index α between two frequencies is given by

$$\alpha = \frac{\log(F_1/F_2)}{\log(\nu_1/\nu_2)}. \qquad (2)$$

We defer to I. Heywood et al. (2022) for further information about the data acquisition, reduction, and availability.

3. Results

3.1. The Filaments in Sgr C

Figure 1 shows the 1.284 GHz MeerKAT (I. Heywood et al. 2022) radio continuum image of a nearly 1° long portion of the negative longitude section of the CMZ, centered on Sgr C. The cyan box shows the full FOV of the JWST observations presented in this paper. The MeerKAT emission in the upper half of the figure, most of which originates in the CMZ centered at Galactic latitude $-0°.050$, is dominated by clumps and filamentary structure. This includes CMZ H II regions such as Sgr C and Sgr B1 (latter not shown; see Figure 10 of I. Heywood et al. 2022). Several prominent NTFs such as the "Snake" (see F. Yusef-Zadeh et al. 2024, and references therein) near $l = 359°.15$ and a bright NTF around $l = 359°.45$ adjacent to Sgr C (F. Yusef-Zadeh et al. 1984) are present. In

contrast, there are two foreground H II regions, located at ~3.5 kpc from the Sun, near the bottom of the figure (T. Nagayama et al. 2009), which show a relatively smooth morphology.

Figure 2 shows the environment of the Sgr C H II region in the MeerKAT 1.28 GHz continuum (top) and spectral index at this frequency (bottom). Several prominent NTFs are roughly orthogonal to the Galactic plane. Others, such as the NTF in the lower right (near $l = 359°.32$), are nearly parallel to the Galactic plane. The H II region is surrounded by a network of filaments that partially wrap around it. The dominant orientation is at Galactic position angle (GPA) GPA ~ 60∘ to 75∘ (GPA is defined as the 0 toward Galactic north and 90∘ along the Galactic plane toward positive Galactic longitudes), similar to the large-scale field toward the CMZ found by A. Mangilli et al. (2019).

The Sgr C H II region, marked by the large oval in Figure 2, has an elliptical shape of ~2′.5 by 3′.4 (5.8 by 8.1 pc) in diameter in the MeerKAT images. The total flux in this area at 1.28 GHz is ~6.68 Jy, and the mean surface brightness (SB) is SB(1.28) = 0.278 mJy arcsec^{-2}. The spectral index in the 1.28 GHz frequency range in the oval is negative, with a value of -0.48 (with an error of ~±0.05), indicating nonthermal synchrotron emission. However, this region includes emission from the bright NTF left from the center of Sgr C. Excluding this NTF increases the index to about -0.38 to -0.41, with some spots having values as high as -0.2 (with an average error of ~±0.05). The 1.28 GHz morphology and spectral index indicates that there is extended nonthermal emission toward the Sgr C H II region. The nonthermal emission may be in front, behind, or comingled with the thermal plasma.

Figure 3 shows a continuum-subtracted, 4.05 μm Br α image of Sgr C (top panel), the ALMA 97 GHz continuum image using only the 12 m antenna data (middle panel), and the MeerKAT 1.28 GHz emission (bottom panel), all with the same
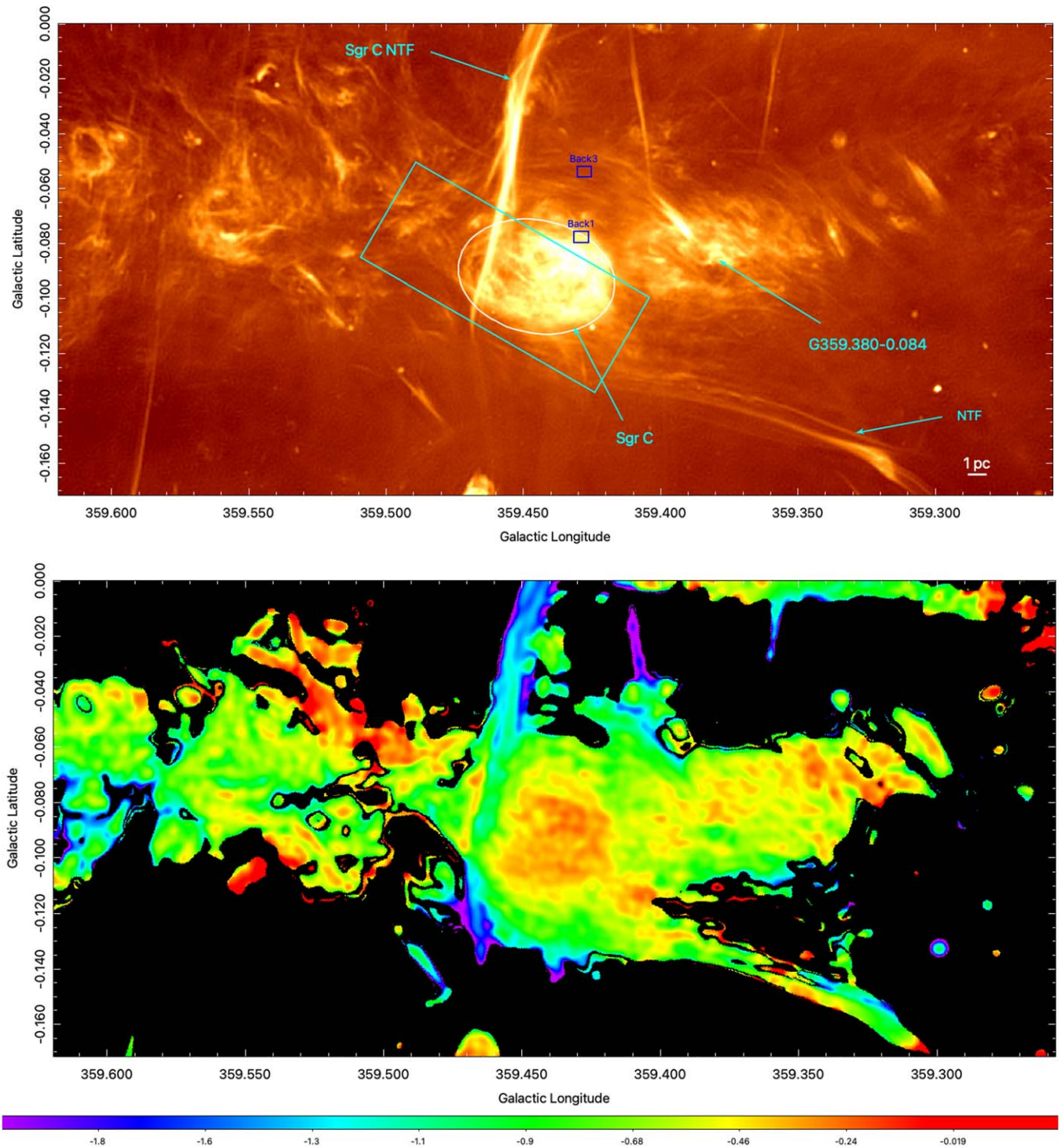
Figure 2. Top: Close-up of the MeerKAT radio continuum image at 1.28 GHz (I. Heywood et al. 2022) showing the environment of the Sgr C H II region. The cyan boxes labeled Back1 and Back3 are used for background subtraction in the 97 to 1.28 GHz spectral index measurements (Section 4). Back2 is a smaller box near the core of the H II region and is shown in Figures 4 and 5. Bottom: MeerKAT spectral index around 1.28 GHz.

FOV. The Br α emission from the H II region is dominated by filamentary structure. Among the brightest filaments, some are nearly parallel to the Galactic plane, while others are nearly at right-angles, hence roughly orthogonal to the plane, similar to the toroidal and poloidal components of the magnetic field (F. Yusef-Zadeh et al. 2004; A. Mangilli et al. 2019; I. Heywood et al. 2022). This phenomenon is examined quantitatively

in Section 3.2. Additionally, there is a population of fainter filaments that tends to point away from the cometary molecular cloud, seen in silhouette against the Br α emission in the top panel of Figure 3. This panel also shows contours of velocity integrated HNCO emission near 87.9 GHz in steps of 2 Jy beam^{-1} taken from the ACES survey. The widths of the filaments range from less than $0\overset{''}{.}15$ (the resolution of JWST at

4
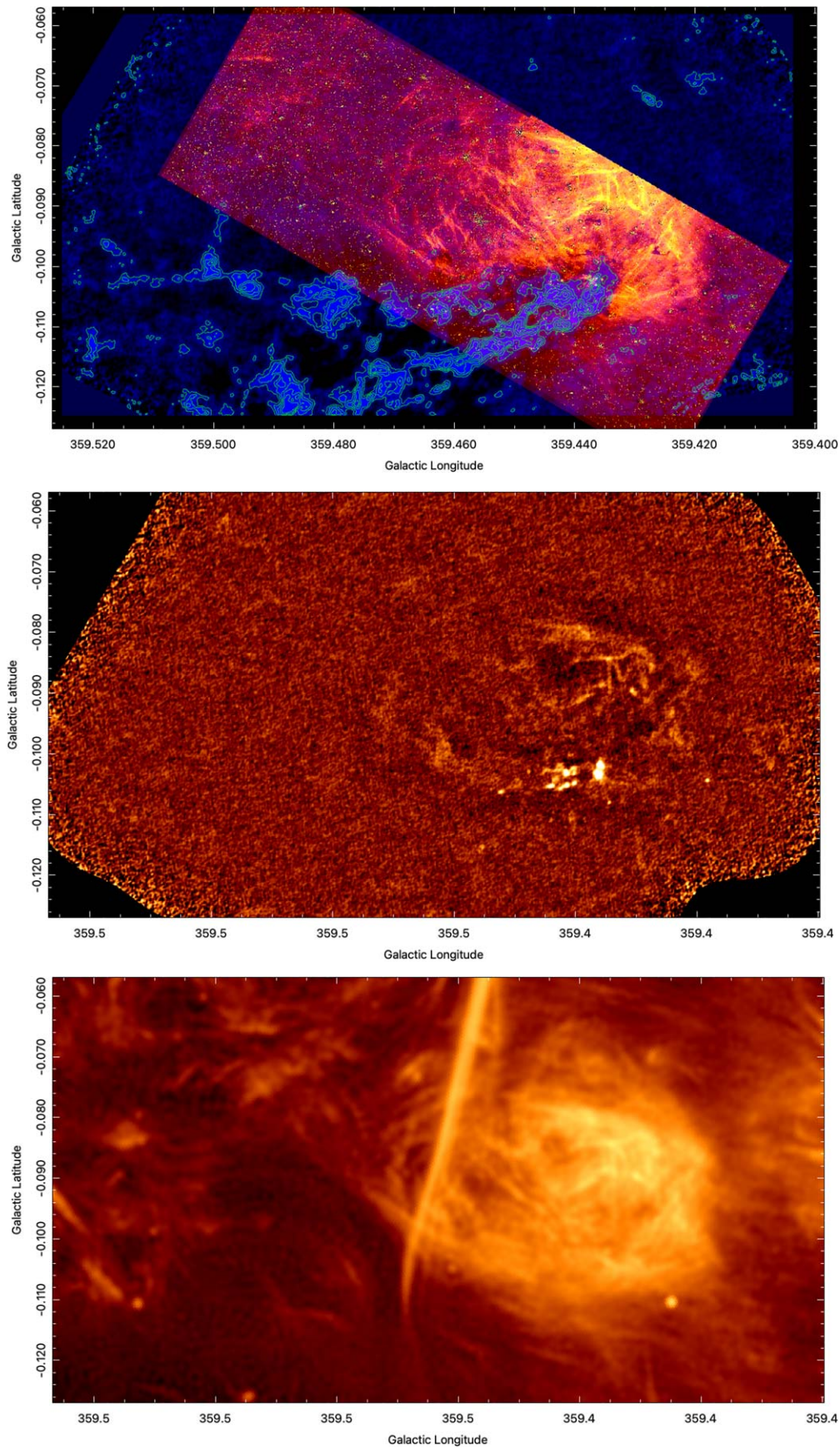
Figure 3. Top: Br α emission in the JWST field. Note the bright "π-shaped" filaments around [359.434, −0.086]. Blue emission and green contours show the intensity of integrated 89.9 GHz transition of HNCO in Jy beam^{-1}. The HNCO map is integrated over a radial velocity range of 41.6 km s^{-1} centered at $V_{\mathrm{LSR}} = -60$ km s^{-1}. Contour levels range from 2 to 10 Jy beam^{-1} in steps of 2 Jy beam^{-1}. The beam FWHM is $1\rlap{.}''94 \times 2\rlap{.}''56$. Middle: ALMA Band 3 97 GHz continuum image with the same FOV as the top panel. Bottom: MeerKAT 1.28 GHz radio continuum image with the same FOV as the above panels.
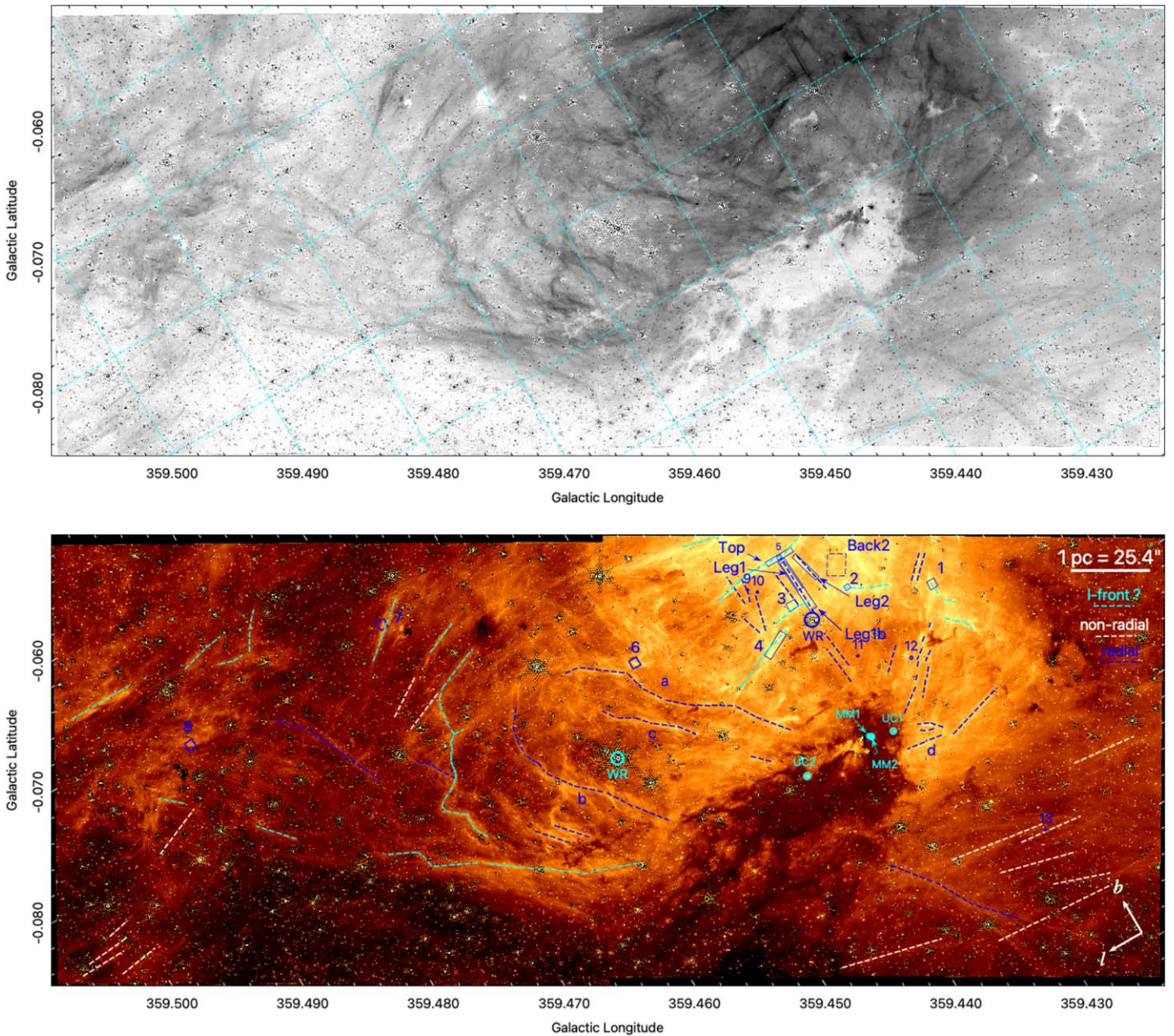
Figure 4. Top: The JWST Br α image, showing the entire field, optimized to show the fainter filaments away from the H II region core. Bottom: The Br α image showing some of the various types of filaments discussed in the text, color-coded according to the legend shown in the upper right corner. Small, cyan circles show compact H II regions in the Sgr C cloud core. Dashed blue line segments mark filaments mostly pointing away from the Sgr C cloud core. Cyan filaments trace concentric arcs around the H II region, and suspected to trace ionization fronts (I-fronts). Dashed, white line segments mark filaments outside the suspected boundaries of the Sgr C H II region. Blue rectangles and squares show measurement boxes used for radio flux measurements. The dashed-blue box marks the reference field Back2. These regions are listed in Table 1. The Br α measurements were made using smaller boxes within some of these regions and are shown in the Appendix. Blue and cyan circles with "WR" underneath mark the locations of the two Wolf–Rayet stars discussed in the text.

4.05 μm) to about 2″ (1000 to 16,000 au) with the majority being near the resolution limit of JWST. Most filaments have lengths ranging from 10″ to over 100″ (0.4 to 4 pc).

The middle panel in Figure 3 shows the 97 GHz continuum emission. Extended emission on scales larger than about 30″ is resolved out. An elliptical ring of emission traces the outer boundary of the H II region. The bright compact sources along the bottom edge trace protostars embedded in the cometary head of the molecular cloud (X. Lu et al. 2020; Paper I). While the (interferometric) ALMA data resolves out most of the extended structure of the Sgr C H II region, the most prominent filaments evident in the JWST Br α images are easily visible.

The bottom panel shows the MeerKAT 1.28 GHz image at the same scale. Because of the ~4″ resolution, some of the filaments seen in the Br α and 97 GHz images are unresolved. However, many are still visible, especially in the extended area around the H II region.

Figure 4 shows Br α emission over the entire field of imaged by JWST in gray scale (top) and pseudocolor (bottom). This figure shows that most of the Br α emission originates in an extensive network of filaments. A sample of filaments are marked by dashed line segments. The cyan segments indicate suspected ionization fronts. These are among the brightest extended Br α features. Most face the Sgr C cloud core where four compact but well-resolved Br α features are suspected to
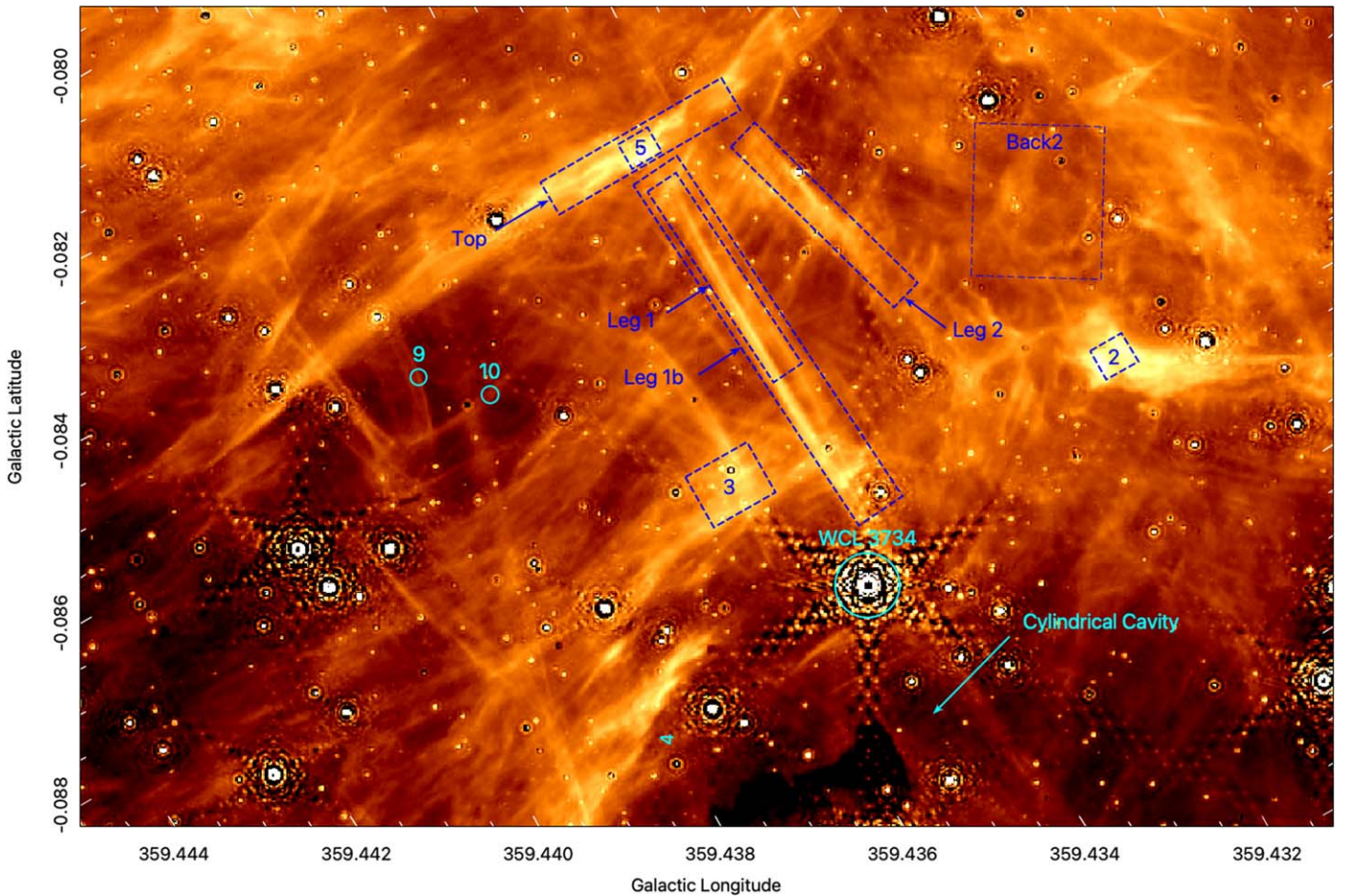
Figure 5. A close-up view of the Br-α emission from the π-shaped filaments and the cylindrical cavity centered on the Wolf–Rayet star WCL 3734.

trace compact H II regions (cyan circles marked as UC1, MM1, MM2, and UC2 from right to left; X. Lu et al. 2019; Paper I), or one of the two WR stars marked in the figure. Suspected ionization fronts tend to have complex, clumpy morphology with relatively sharp edges facing the nebular core with a more gradual decline of intensity in the opposite direction. The blue boxes marked 1 through 5 are examples. These features trace a segmented arc with a radius of about 1.8 pc and centered on the region hosting the suspected compact H II regions. Cyan segments and the box labeled 5 appear to trace another ionization front about 2.8 pc from the cloud core. The JWST field missed a portion of the H II region near the top of the field. Figure 3 shows that the upper-edge of the H II region extends beyond the JWST field to a radius of about 3 pc from the core. A portion of a suspected ionization front at a radius of ∼3.5 pc is marked by a cyan segment just above the label "Top." The jagged cyan line near longitude 359°.470 (note that tick marks in the figure are tilted because the JWST field is rotated with respect to Galactic coordinates) may trace a more distant ionization front located about 5.2 pc from the core. Region 7 and the associated cyan arc trace a ∼1 pc-long filament of Br α emission that faces the H II region that may trace the most distant ionization front from the Sgr C core so far recognized. It is located 6.2 pc from the core. The Br α emission around Legs 1 and 2 and Top form a π-shaped structure just above the WR star WR3734. The mean Br α intensity diminishes with increasing distance up to about 5 or 6 pc from this region.

Comparison of the Br α image with the 1.28 GHz MeerKAT image shows that the "Top" of the π-shaped filament extends beyond the JWST field toward the upper right. There is a coherent network of fainter filaments throughout the JWST field outside the suspected ionization fronts.

Figure 5 presents a close-up view of the π-shaped structure consisting of Leg 1, Leg 2, and Top. The regions labeled 2, 5, and Top (region 5 is the brightest portion of the "Top" filament) may trace ionization fronts. However, the feature labeled "Leg 1" has a much smoother appearance and is remarkably straight. It can be traced for nearly $90''$ (3.5 pc) from "Top" to nearly the edge of the Sgr C cloud. It consists of several parallel strands extending over about a $1''$ to $2''$ (0.04 to 0.08 pc) wide region. Each strand has a width of about $0.''1$ to $0.''3$ (0.004 to 0.01 pc). A filament about $3''$ (0.1 pc) left of this bundle runs nearly parallel but is shorter. This feature crosses a suspected ionization front in region 3. Region 9 marks the right side of a set of V-shaped filaments ranging in length from 0.2 to 0.4 pc running parallel to Leg 1. As with Leg 1, these filaments also consist of multiple strands barely resolved on the JWST images. These filaments are nearly orthogonal to the Galactic plane. A network of fainter filaments runs nearly parallel to the plane and the suspected ionization front marked by "Top." Region 10 marks one of these filaments.

These data stand in stark contrast with hydrogen recombination line (Hα) and radio continuum images of H II regions near the Sun and in the Galactic disk away from the CMZ, which tend

to show mostly smooth plasma morphologies (see, e.g., the two foreground H II regions in Figure 1). Although in nearby H II regions, such as the Orion Nebula, some filaments are seen (F. Yusef-Zadeh 1990; C. R. O'Dell 2001), these structures either are ionization fronts, such as the Orion Bar, or are highly tangled, unlike the filaments in the Sgr C Br α image.

3.2. Filament Orientations

To assess the orientation of the Br α filaments with respect to the dominant poloidal and toroidal components of the CMZ magnetic field, a statistical analysis was performed using the `fil_finder` algorithm (E. W. Koch & E. W. Rosolowsky 2015). This algorithm is typically used for longer wavelength imaging of molecular clouds (e.g., with Herschel far-IR and ALMA millimeter imaging, S. Biswas et al. 2024; K. Tachihara et al. 2024; J. W. Zhou et al. 2024) or in analysis of cloud simulations (e.g., E. Mullens et al. 2024). Here, we present a novel application of the algorithm for identifying filaments in shorter wavelength ($\lambda \sim 4~\mu m$) hydrogen recombination line emission that could be generalized for use in any region of filamentary ionized gas, in the CMZ or elsewhere.

Following instructions in the `fil_finder` tutorial,[12] a mask was first constructed on the brightest portion of the Sgr C H II region with the following parameters: `glob_thresh` (i.e., minimum intensity) of 20 MJy sr^{-1}, `size_thresh` of 1000 pix^2, and `adapt_thresh` of 0.05 pc. These parameters were chosen to reflect the typical size and brightness of filaments in the Br α image, such that most of the visually identifiable filaments were recovered by the algorithm. We note that several parameter combinations were explored, and that the overall trend of filament orientations (bottom panel of Figure 6) was found to be insensitive to different parameter choices.

This mask was then used to construct a "skeleton" consisting of 1 pixel wide representations of each filament. A rolling Hough transform (RHT; S. E. Clark et al. 2014) was performed on each branch of each filament in the skeleton, with a minimum branch length `min_branch_length` of 30 pix., or ~10 resolution elements in the Br α image. This returns the orientation of the Br α filament. We note that an orientation could not be measured with the RHT for every filament identified by `fil_finder`, likely in cases where, for example, the filament curvature was too high (or its structure too tangled) for the RHT to retrieve a physical result. Therefore, the results presented in Figure 6 are only for the filaments for which an orientation value was retrieved. The distribution of these filament orientations, weighted by a factor of filament intensity times' filament width, is presented in Figure 6.

Bright stars exhibit strong diffraction artifacts, mostly produced by the straight edges of the hexagonal elements comprising JWST's 6.5 m primary mirror. These show up as chains of spots in the Br α image at GPA of $-30°$, $30°$, and $90°$. However, because the Br α image has been continuum subtracted, these artifacts consist of discrete dark and light spots, i.e., regions of positive and negative fluxes, because of the difference in point-spread function between F405N, F360M, and F480M (the latter two being the "continuum" filters used for subtraction). Therefore, the `fil_finder` algorithm does not appear to detect them (see the middle panel of Figure 6). Nevertheless, the orientation of these

artifacts are marked by dashed lines in the bottom panel of Figure 6.

There appears to be a peak in the filament orientation distribution centered at GPA ~ 0°, or aligned with Galactic north. This reflects the poloidal component of the CMZ magnetic field (i.e., perpendicular to the galactic plane; M. Morris 2007), which is also observed in the typical orientations of NTFs seen in radio images of the CMZ (F. Yusef-Zadeh et al. 2004; I. Heywood et al. 2022). To quantify the significance of this peak in the distribution of filament orientations, we calculate the "projected Rayleigh statistic" (see Equation (6) and Equation (7) of D. L. Jow et al. 2018) of the distribution. We find a strongly positive value of $Z_x = 5.8 \pm 0.9$, indicating significant alignment around GPA ~ 0°, i.e., close to orthogonal to the Galactic plane.

Besides the peak in filament orientations around GPA = 0°, there does not appear to be any other similarly strong preferential orientation of the Br α filaments; i.e., there is no evidence of a multimodal distribution. This is quantitatively supported by the fact that $Z_x \gg 0$, which indicates strong alignment only near GPA = 0° (D. L. Jow et al. 2018). This may reflect the preferential orientation of many filaments with respect to the Sgr C molecular cloud, appearing to point either radially away from the cloud or parallel to the cloud's edge as ionization fronts (see the bottom panel of Figure 4). This would have the effect of "blurring out" any other subtler systematic orientations due to, e.g., the toroidal component of the CMZ magnetic field. Nonetheless, the preferential alignment of some Br α filaments at GPA ~ 0° indicates that there is a population of filaments whose morphology has been strongly influenced by the global CMZ poloidal magnetic field component. However, the large spread of orientations implies that there are other populations of filaments whose orientation is sculpted in a larger part by interactions with the Sgr C molecular cloud, e.g., as ionization fronts.

3.3. Physical Parameters from Br α

In this section, we derive physical parameters, including the Br α SB, the plasma emission measure (EM), and the electron density of various features such as suspected ionization fronts and filaments in the continuum-subtracted Br α image. The intensities of most emission lines, such as the hydrogen recombination lines and the free–free radio continuum emission, are proportional to the EM. EM is defined as
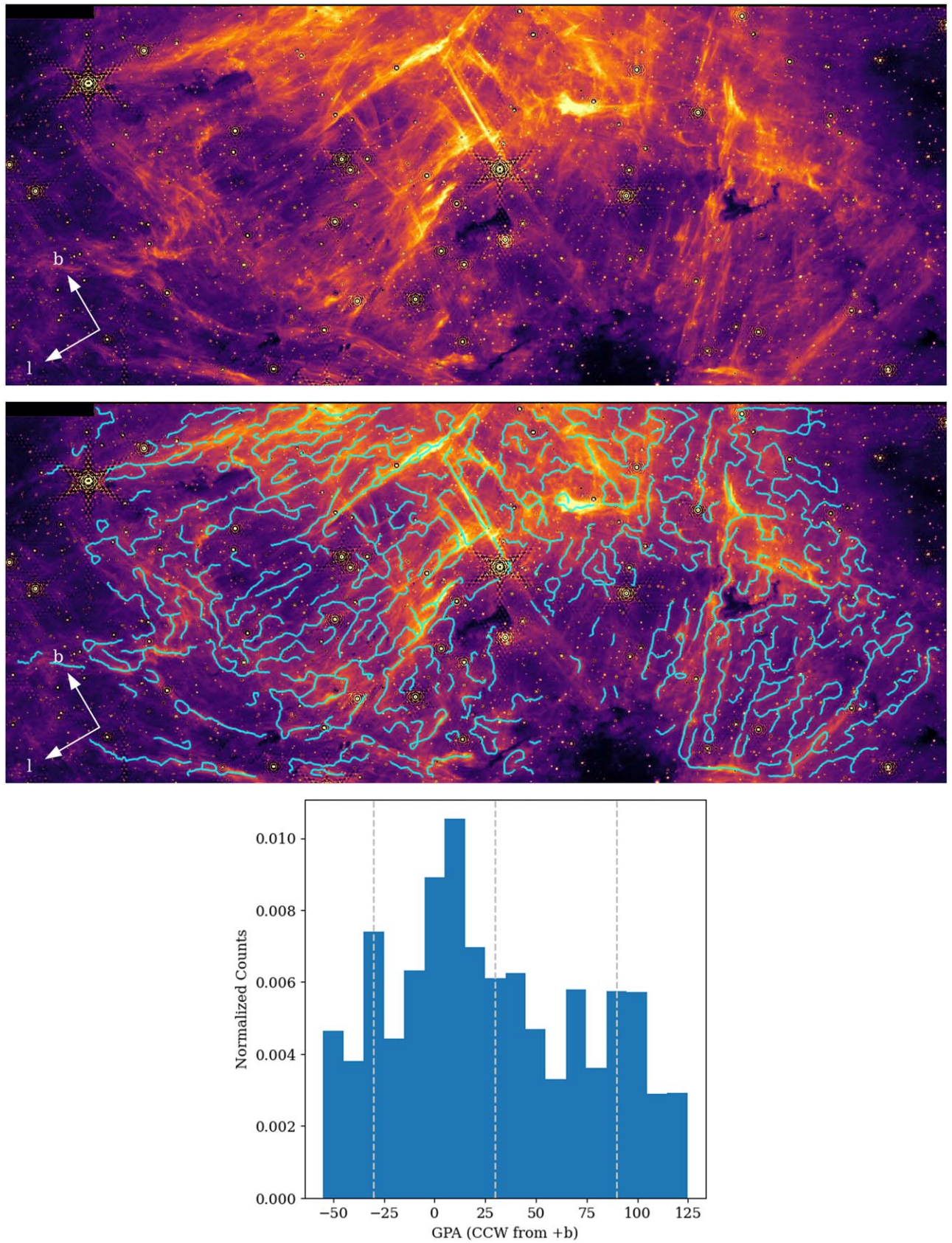
$$\mathrm{EM} = \int n_e^2 dl \simeq n_e^2 L$$

specified in units of cm^{-6} pc, where n_e is the electron density, dl is a distance element along our line of sight (LOS) through the emission region, and L is the effective total path length in parsecs.

For calculating EMs, the native JWST pixel values, given in units of MJy sr^{-1}, had to be converted to the more conventional SB units, ergs per second per squared centimeter per squared arcsecond. 1 MJy sr^{-1} corresponds to 2.350443×10^{-5} Jy arcsec^{-2}. The conversion of Janskys to units of SB requires multiplication by bandwidth of the filter in Hertz in order to eliminate the Hz^{-1} in the definition of a Jansky. The JWST F405N filter has a 0.046 μm passband,[13] which corresponds to

---

[12] https://fil-finder.readthedocs.io/en/latest/tutorial.html

[13] https://jwst-docs.stsci.edu/jwst-near-infrared-camera/nircam-instrumentation/nircam-filters

Figure 6. Top: NIRCam Brα image of the brightest portion of the Sgr C H II region (see Figure 4). Middle: identical image to the top panel with the addition of the filaments and branches identified by the `fil_finder` algorithm plotted in cyan. Bottom: Normalized histogram, with 10° bins, of Br α filament Galactic position angle (GPA; defined in the text), weighted by a factor consisting of filament intensity multiplied by filament length. Dashed, vertical lines indicate the orientations of the diffraction spikes in the Br α image.

Table 1
Regions Used for Radio and Br α Flux Measurements

Region	Longitude (deg)	Latitude (deg)	Dimensions (arcsec)	GPA (deg)
H II	359.4450	−0.0922	73.82 × 103.48	78
Leg 1	359.4345	−0.0863	1.57 × 10.41	3
Leg 1b	359.4344	−0.0872	2.39 × 18.64	3
Leg 2	359.4330	−0.0863	1.57 × 10.41	15
Top	359.4355	−0.0843	9.54 × 1.71	0
1	359.4239	−0.0928	0.130 × 1.120	0
1b	359.4242	−0.0928	0.130 × 1.120	0
2	359.4309	−0.0896	0.384 × 0.707	0
2b	359.4306	−0.0896	0.258 × 0.693	0
3	359.4357	−0.0886	3.23 × 2.64	0
4	359.4388	−0.0909	9.28 × 2.42	28
5	359.4346	−0.0844	1.57 × 1.31	0
6	359.4504	−0.0860	0.94 × 0.94	circle
7	359.4679	−0.0719	1.956 × 0.226	328
8	359.4878	−0.0727	0.527 × 0753	328
9	359.4385	−0.0855	⋯	peak pixel
10	359.4378	−0.0861	⋯	peak pixel
11	359.4329	−0.0954	⋯	peak pixel
12	359.4289	−0.0979	⋯	peak pixel
13	359.4263	−0.1171	⋯	peak pixel
Back 1	359.4288	−0.0779	18.67 × 13.99	0
Back 2	359.4305	−0.0875	6.97 × 5.94	58
Back 3	359.4276	−0.0541	18.67 × 13.99	0

a bandwidth of $\Delta\nu = 8.395 \times 10^{11}$ Hz. Thus, 1 MJy sr^{-1} corresponds to an SB 1.971×10^{-16} erg s^{-1} cm^{-2} arcsec^{-2}.

Two corrections must be applied to the raw Br α SB estimates before computation of the EMs and electron densities. First, the background emission in the immediate vicinity of a feature, which presumably originates in front or behind the emission region under consideration, must be subtracted. Second, the fluxes must be corrected for extinction.

Measurement of the fluxes and physical properties of various compact features and filaments require careful background subtraction because of emission along the LOS that is unrelated to the feature under consideration. For each feature, elongated measurement boxes ("DS9 region files") are used "on" and "off" the suspected feature. The "off" positions are taken to be a similar sized region deemed to be free from emission from the feature, determined uniquely for each feature. The resulting fluxes and derived parameters are therefore sensitive to the choice of "off" region used for background subtraction. The uncertainty in the measured fluxes is estimated to be about 20%–30% based on the typical range of background fluxes around each region. The high density of stars in the CMZ fields is the major source of this uncertainty. In the continuum-subtracted images, bright stars leave large residuals, and fainter stars are poorly subtracted due to their color variations. We list the coordinates of the fields for which measurements were made in Table 1, their areas, and orientations. The positions used to estimate nearby background fluxes are shown in the figures in Appendix. Because of the vastly different resolution of the radio and Br α images, different regions are used for the infrared and radio measurements.

In Table 1 the first entry, "H II," corresponds to the large oval shown in Figure 2 encompassing the entire Sgr C H II region. The dimensions listed give the semimajor and semiminor axes of the ellipse. The next four entries (Leg 1, Leg 1b, Leg 2, and Top) correspond to rectangular apertures shown in Figure 4,

which mark the "π-shaped" group of filaments located near the top of the JWST Br α image in the brightest portion of the H II region. The numbered entries correspond to bright features also marked on Figure 4. Entry 5 is located inside the rectangle "Top" delineating the top of the π-shaped filaments. Regions 3 to 13 correspond to other features discussed below. The final three regions, Back1, Back2, and Back3, refer to areas where backgrounds were measured on the MeerKAT 1.28 GHz image. Magnified views of subfields in the Br α image are shown in Appendix along with the locations of various regions used for Br α measurements listed in Table 1. The physical properties of some selected filaments, suspected ionization fronts, and other features are tabulated in Table 2 and discussed below.

F. Nogueras-Lara (2024) measured the near-infrared reddening to thousands of stars to create a map of the 2.15 μm K_s extinction toward the Sgr C H II region (see their Figure 3). F. Nogueras-Lara (2024) find that the extinction in the K_s filter varies from $A_{K_s} \sim 2.0$ to 2.5 mag toward the H II region, but reaches values larger than 3 mag toward the Sgr C molecular cloud, which appears nearly opaque in the Br α image. Around the brightest part of the nebula, containing the π-shaped filaments, $A_{K_s} \sim 2.0$ mag. We scale the 2.15 μm extinction to the 4.05 μm wavelength of the Br α emission line using the relation $A_\lambda \propto 1/\lambda$ (E. L. Fitzpatrick 1999). Thus, $A_{4.05\mu m} \approx 0.529 A_{K_s}$. The extinction corrected SB values, SB, are related to the raw SB measurements, SB$_o$, by

$$\text{SB} \approx \text{SB}_o \; 10^{0.529 A_{K_s}/2.5},$$

which implies scaling by a factor $f = 2.65$ to 4.31 for $A_{K_s} = 2$ to 3 mag. Uncertainties in the reddening correction due to incomplete knowledge of the extinction curve in the CMZ and spatial variations introduce uncertainties in the extinction corrected values. If a CMZ extinction law of $A_\lambda \propto 1/\lambda^{1.5}$ was instead adopted, similar to more recent extinction measurements toward the CMZ (see S. Nishiyama et al. 2009; T. K. Fritz et al. 2011, noting the uncertainties in the extinction curve between ~2 and 4 μm due to the presence of several prominent emission features), each Br α SB measurement would decrease by ~23% (and the corresponding electron density, thermal pressure, and plasma β by ~12%). Thus, the adopted extinction law of $A_\lambda \propto 1/\lambda$ may be a conservative overestimation of the strength of thermal pressure (Equation (3)) in the Sgr C H II region.

The EM is related to the intensity of the visual wavelength ($\lambda = 6563$ Å) Balmer-alpha (Hα) emission line,

$$\text{EM} = 3.975 \times 10^{17} \text{I}(\text{H}_\alpha)(\text{cm}^{-6} \text{ pc})$$

where I(Hα) is in ergs per second per squared centimeter per squared arcsecond units (L. M. Haffner et al. 2003). We use the Case B hydrogen recombination spectrum to relate the expected intensity of Br α to Hα at 5000 and 10,000 K. Using Table 14.2 in (B. T. Draine 2011), we find that I(Hα)/I(Br α) = 29.6023 at 5000 K and 36.0833 at 10,000 K. At these two plasma temperatures, the EM is given by EM = 1.1766×10^{19}I(Br$_\alpha$) at $T = 5000$ K and EM = 1.4343×10^{19}I(Br$_\alpha$) at $T = 10,000$ K. Interpolating to 6000 K (which we take to be the typical H II region temperature in the CMZ; J. E. Wink et al. 1983;

Table 2
Physical Parameters of the Brightest Features Derived from the Br α Image

Region	Counts (MJy sr^{-1})	Corrected SB (erg s^{-1} cm^{-2} as^{-2})	L (pc)	EM (cm^{-6} pc)	n_e (cm^{-3})	P_{ii} (dynes cm^{-2})	β	Comments
Sgr C ($A_{Ks}=2$)	25.1	1.53e-14	5.83	1.88e+05	179	2.97e-10	0.0075	Entire H II region
Sgr C ($A_{Ks}=3$)	25.1	1.95e-14	5.83	3.06e+05	229	3.80e-10	0.0095	
L1 ($A_{Ks}=2$)	50.1	2.62e-14	0.00966	3.22e+05	5770	9.56e-09	0.24	π-leg
L1 ($A_{Ks}=3$)	50.1	4.27e-14	0.00966	5.24e+05	7367	1.22e-08	0.307	
L1 peak	83.8	4.38e-14	0.00966	5.37e+05	7459	1.24e-08	0.311	
	83.8	7.13e-14	0.00966	8.76e+05	9524	1.58e-08	0.397	
L2	37.3	1.95e-14	0.00848	2.39e+05	5312	8.8e-09	0.221	π-leg
	37.3	3.18e-14	0.00848	3.9e+05	6782	1.12e-08	0.282	
L2 peak	51.8	2.71e-14	0.00848	3.32e+05	6260	1.04e-08	0.261	
	51.8	4.41e-14	0.00848	5.42e+05	7992	1.32e-08	0.333	
1	72.3	3.78e-14	0.00511	4.64e+05	9532	1.58e-08	0.397	I-front
	72.3	6.16e-14	0.00511	7.56e+05	12,170	2.02e-08	0.507	
1b	49.4	2.58e-14	0.00511	3.17e+05	7879	1.31e-08	0.328	I-front
	49.4	4.21e-14	0.00511	5.17e+05	10,060	1.67e-08	0.419	
2	215	1.12e-13	0.0151	1.38e+06	9564	1.58e-08	0.398	Cometary I-front
	215	1.83e-13	0.0151	2.25e+06	12,210	2.02e-08	0.508	
2b	158	8.24e-14	0.0105	1.01e+06	9805	1.62e-08	0.408	Second I-front
	158	1.34e-13	0.0105	1.65e+06	12,520	2.07e-08	0.521	
3	55.2	2.88e-14	0.00785	3.54e+05	6715	1.11e-08	0.28	Tilted I-front
	55.2	4.7e-14	0.00785	5.77e+05	8574	1.42e-08	0.357	
4	103	5.36e-14	0.0075	6.58e+05	9366	1.55e-08	0.39	I-front
	103	8.73e-14	0.0075	1.07e+06	11,960	1.98e-08	0.498	
5	133	6.95e-14	0.00617	8.54e+05	11,770	1.95e-08	0.49	I-front
	133	1.13e-13	0.00617	1.39e+06	15,030	2.49e-08	0.626	
T	104	5.43e-14	0.00754	6.67e+05	9407	1.56e-08	0.392	Top of π
	104	8.86e-14	0.00754	1.09e+06	12,010)	1.99e-08	0.5	
6	40.8	2.13e-14	0.00785	2.62e+05	5773	9.56e-09	0.24	WR 4083 shell ?
	40.8	3.47e-14	0.00785	4.27e+05	7371	1.22e-08	0.307	
7	17.4	9.09e-15	0.00903	1.12e+05	3516	5.82e-09	0.146	Outer H II
	17.4	1.48e-14	0.00903	1.82e+05	4489	7.44e-09	0.187	
8	13.5	7.05e-15	0.0208	8.66e+04	2040	3.38e-09	0.0849	Left edge
	13.5	1.15e-14	0.0208	1.41e+05	2605	4.32e-09	0.108	
9	14	7.31e-15	0.0102	8.98e+04	2966	4.91e-09	0.124	
	14	1.19e-14	0.0102	1.46e+05	3787	6.27e-09	0.158	
10	8	4.18e-15	0.0102	5.13e+04	2242	3.71e-09	0.0934	
	8	6.81e-15	0.0102	8.37e+04	2863	4.74e-09	0.119	
11	4	2.09e-15	0.0314	2.57e+04	903.8	1.5e-09	0.0376	
	4	3.41e-15	0.0314	4.18e+04	1154	1.91e-09	0.0481	
12	13.5	7.05e-15	0.0314	8.66e+04	1660	2.75e-09	0.0691	
	13.5	1.15e-14	0.0314	1.41e+05	2120	3.51e-09	0.0883	
13	3.01	1.57e-15	0.0314	1.93e+04	784	1.3e-09	0.0326	
	3.01	2.56e-15	0.0314	3.15e+04	1001	1.66e-09	0.0417	

D. S. Balser et al. 2011) gives

$$\text{EM} = 1.2282 \times 10^{19} I(\text{Br}_\alpha) \, (\text{cm}^{-6} \, \text{pc})$$

where the Br α intensities are the extinction-corrected values. The mean and peak electron densities are derived by assuming that the LOS depth of a feature, L, is identical to the projected width on the plane of the sky, corrected for the resolution of JWST. Thus,

$$n_e \approx \sqrt{\frac{\text{EM}}{L}} \quad (\text{cm}^{-3}).$$

This approximation works for cylindrical structures, but for edge-on or inclined sheets or bubbles, it will underestimate L and overestimate n_e.

The plasma thermal pressure, P_T, defined as

$$P_{ii} = 2 n_{ii} k T_{ii} \qquad (3)$$

where the factor of 2 accounts for the contribution of both protons and electrons to the pressure in terms of the electron density n_{ii}, k is the Boltzmann constant, and T_{ii} is the plasma temperature, which we take to be 6000 K (J. E. Wink et al. 1983; D. S. Balser et al. 2011). The plasma β parameter is a measure of the importance of magnetic fields for the dynamics of the plasma. The plasma β is defined as

$$\beta = P_T / P_B \qquad (4)$$

where P_T is the thermal pressure (Equation (3)), and P_B is the magnetic pressure,

$$P_B = \frac{B^2}{8\pi} \qquad (5)$$

where B is the magnetic field strength. For the analysis here, we assume that the magnetic field has a strength of 1 mG in every

Table 3
Physical Parameters of Compact H II Regions

Region	Counts (MJy sr^{-1})	Corrected SB (erg s^{-1} cm^{-2} as^{-2})	L (pc)	EM (cm^{-6} pc)	n_e (cm^{-3})	M ($M_\odot$)	Q (s^{-1})	Comments
UC 1	69	0.6×10^{-13}	0.027	0.72×10^6	5180	0.0017	3.2e45	Cometary
mm1	160	1.4×10^{-13}	0.021	1.67×10^6	8856	0.0015	4.6e45	Barely resolved
mm2	137	1.2×10^{-13}	0.045	1.43×10^6	5640	0.0090	1.8e46	Extended halo
UC 2	54	0.5×10^{-13}	0.045	0.57×10^6	3541	0.0056	6.9e45	Extended halo

Note. The errors on SB and EM are estimated to be about 20% to 30%, due to the choice of apertures used to measure the compact H II region fluxes. An extinction of $K_s = 3$ mag is assumed. If the extinction is higher, the values presented here are lower bounds.

region, the typical large-scale average field strength in dense CMZ clouds (K. Ferrière 2009; T. Pillai et al. 2015).

Table 2 lists measurements derived for selected regions. The first column gives the identity of the region as marked in the figures. Column 2 gives the locally *background subtracted* mean counts in each measurement box in MJy sr^{-1}. Column 3 gives the extinction corrected SB of the Br α emission. Column 4 gives the assumed LOS path-length, L, taken to be equal to the minor-dimension width of the feature on the plane of the sky. Column 5 gives the EM. Column 6 is the derived electron density n_e for the assumed path length, L. Column 7 lists the resulting plasma thermal pressure, P_T. Column 8 gives the plasma β parameter. For each region, we evaluate the parameters for two values of extinction, corresponding to $A_{K_s} = 2$ mag (first row for each region) and $A_{K_s} = 3$ mag (second row).

3.4. Sgr C H II Region Parameters

We first discuss the average properties of the Sgr C H II region, measured by summing the background-subtracted Br α flux from the portion of Sgr C in the JWST NIRCam field. An elliptical region with semiminor and semimajor radii of 74″ and 103″ was used for this measurement. For estimation of the electron density, we use 2 times the semiminor radius as an estimator of the LOS depth of the H II region. Thus, $L_{ii} = 148″$ or 5.83 pc. The harmonic mean radius, $R_{ii} \sim 87″$ (3.45 pc), was used to estimate the mass of plasma and the hydrogen-ionizing Lyα luminosity of the H II region.

We use the continuum-subtracted Br α image to estimate the mean value of the pixel counts in the 148″ by 206″ diameter elliptical region, finding a mean SB value of ~25.2 MJy sr^{-1}. Faint Br α emission with a mean value of about ~3 MJy sr^{-1} is seen throughout the JWST field beyond the suspected, projected boundaries of the Sgr C H II region. The background plus foreground contribution to the flux, measured in corners of the Br α image and toward the opaque Sgr C cloud, is ~3 MJy sr^{-1}. The MeerKAT 1.28 GHz image and the extension of the oval region beyond the JWST field show that the Br α image misses about 12% of the projected area of the H II region. However, the exclusion of this field does not contribute to the mean counts in the measurement oval. Comparison of the MeerKAT and Br α images shows that the Sgr C cloud obscures about 12% of the area and flux in the measurement oval. Thus, to get a better estimate of expected mean flux from the H II region, we scale the background-subtracted mean value (25.2 − 3 = 22.2 MJy sr^{-1}) by a factor of 1.12, yielding a mean flux density in the oval, 24.9 MJy sr^{-1}.

We also used a measurement box that avoids the Sgr C molecular cloud and associated extinction, but covers a similar area as the measurement oval, yielding a background-subtracted mean flux density of 29.6 MJy sr^{-1}. We use the mean of these two measurement methods to estimate the raw (reddened) flux and use the difference as an estimator of the systematic error. Thus, the best estimate of the raw, mean SB density, from the Sgr C H II region, without correction for foreground extinction, is 27.2 ± 2.4 MJy sr^{-1}. The subtraction artifacts surrounding bright stars, and the contribution of residual emission from fainter stars render this estimate uncertain by about 10%, smaller than the 20% to 30% error for the small measurement regions used for the filaments and ionization fronts.

For all features within the H II region, we assume that the foreground K_s (2.15 μm) extinction is either 2 or 3 mag (F. Nogueras-Lara 2024). Thus, this mean SB density is scaled by a factor of 2.65 or 4.32 before being converted into SB units. The EM across the entire H II region is EM ≈ 1.75×10^5 cm^{-6} pc, for $A(K_s) = 2$ mag or EM ≈ 2.85×10^5 cm^{-6} pc, for $A(K_s) = 3$ mag. Thus, the estimated mean electron density is $n_e \approx (EM/L_{ii})^{1/2} = 173$ to 221 cm^{-3} for $A(K_s) = 2$ to 3 mag, lower than the 300 cm^{-3} quoted by J. P. Simpson (2018).

For an effective radius of $R_{ii} = 3.45$ pc, the H II region plasma mass is about between 992 $M_\odot$ to 1266 $M_\odot$ (for $A(K_s) = 2$ to 3 mag). The Lyman continuum luminosity required to maintain photoionization equilibrium in the H II region is estimated to be $Q \approx 0.60$ to 0.97×10^{50} H-ionizing photons per second in the absence of significant dust absorption between the ionizing stars and the outer boundary of the H II region. The plasma β for the H II region as a whole is 0.0072 (0.0092 for $A(K_s) = 3$ mag) assuming a mean field strength of 1 mG.

Table 3 summarizes the properties of the four suspected compact H II regions (X. Lu et al. 2019; Paper I) that were discussed above and marked in the figures.

We derive the same parameters from the MeerKAT 1.28 GHz image under the assumption that all the emission originated from thermal bremsstrahlung (the free–free) process. For a thermal plasma, the flux density in the long-wavelength (Rayleigh–Jeans) limit is given by

$$S_\nu = \frac{2kT_{ii}\nu^2}{c^2}\tau_\nu$$

where S_ν is the total flux density in Jy, T_{ii} is the plasma temperature of the H II region, ν is the frequency, and τ_ν is the free–free optical depth given by

$$\tau_\nu \approx 3.28 \times 10^{-7} \; T_4^{-1.35} \; \nu_{GHz}^{-2.1} \; EM$$

where T_4 is the plasma temperature in units of 10^4 K, and ν_{GHz} is the frequency in units of 1 GHz (P. G. Mezger & A. P. Henderson 1967; J. J. Condon & S. M. Ransom 2016).

Table 4
Spectral Indices of Bright Features from 98 to 1.28 GHz

Component	SB(97) (mJy arcsec^{-2})	SB(1.3) (mJy arcsec^{-2})	SB1(1.3) (mJy arcsec^{-2})	SB2(1.3) (mJy arcsec^{-2})	SB3(1.3) (mJy arcsec^{-2})	α_{raw}	α_1	α_2	α_3
Leg 1	0.182	0.781	0.531	0.233	0.755	−0.336	−0.247	−0.057	−0.328
Leg 1b	0.208	0.794	0.544	0.246	0.768	−0.309	−0.222	−0.039	−0.301
Leg 2	0.256	0.774	0.524	0.226	0.748	−0.255	−0.165	0.029	−0.247
Top	0.458	0.981	0.731	0.433	0.955	−0.176	−0.108	0.013	−0.169
1	0.412	0.657	0.407	0.109	0.631	−0.108	0.003	0.306	−0.098
2	0.813	0.528	0.278	−0.020	0.502	0.100	0.248	⋯	0.111
3	0.459	0.872	0.622	0.324	0.846	−0.148	−0.070	0.080	−0.141
4	0.372	0.693	0.443	0.145	0.667	−0.143	−0.040	0.218	−0.135
5	0.776	1.258	1.008	0.710	1.232	−0.112	−0.061	0.020	−0.107
Back 1	⋯	0.250	0.000	−0.298	0.224	⋯	⋯	⋯	⋯
Back 2	⋯	0.548	0.298	0.000	0.522	⋯	⋯	⋯	⋯
Back 3	⋯	0.026	−0.224	−0.522	0.000	⋯	⋯	⋯	⋯

Thus, the flux density and EM are related by

$$\mathrm{EM} = 1.25 \times 10^5 \quad T_4^{0.35} \quad \nu_{\mathrm{GHz}}^{0.1} \quad S_\nu.$$

The flux density of the continuum on the MeerKAT 1.28 GHz images in the same oval region used above is $S_{1.28}$=6.68 Jy. The emission outside the oval region is used to estimate a background SB of about 0.82 Jy in the same area, yielding an estimate for the 1.28 GHz flux from the Sgr C H II region of $S_{1.28}$ = 5.86 Jy. Thus, the EM is $\mathrm{EM}_{1.28} = 6.3 \times 10^5 (\mathrm{cm}^{-6}\ \mathrm{pc})$. Using the same LOS path length as above gives an electron density estimate of n_e(1.28 GHz) = 330 cm^{-3}, a plasma mass of about 1915 $M_\odot$, and a Lyman continuum luminosity $Q \approx 2.13 \times 10^{49}$ s^{-1}. The resulting electron densities and masses are about a factor of 1.5 to 1.9 times higher than estimated from the extinction-corrected Br α flux. Given the estimated uncertainties, this is a significant difference. Either the extinction is underestimated, or there is a contribution of nonthermal emission to the 1.28 GHz flux. The latter conclusion is consistent with the nonthermal spectral index at the MeerKAT frequency of 1.28 GHz.

The masses of plasma associated with the ionization fronts and filaments are small. For the densest features, the mass within a spherical region whose diameter is comparable to the projected width of the feature is typically less than 2×10^{-4} $M_\odot$. At an electron density $n_e = 10^4$ cm^{-3}, a 1 arcsec^2 region would have mass of order 0.02 $M_\odot$. A key result from this analysis is that, for a typical (large-scale average) magnetic field strength of 1 mG, even the brightest and most compact features seen in the JWST images are magnetically dominated, with a plasma β less than 1.

3.5. Spectral Indices

To investigate the physical origin of these filaments, the spectral index was measured in the Sgr C H II region. Because of the varying resolution and spatial filtering in the ALMA and MeerKAT data, we measured the spectral indices of compact structures and filaments between 1.28 and 97 GHz by removing the estimated contributions of the extended or unrelated foreground and background low-frequency emission. We selected three measurement boxes in the MeerKAT images for this background removal. "Back1" is located just beyond the outer edge of the H II region, as seen in the 97 GHz ALMA image, but inside the extended envelope of 1.28 GHz emission

surrounding Sgr C region. "Back2" is a smaller box inside the bright core of the H II near the π-shaped filaments, but avoiding any of these filaments. "Back3" is located even farther from Sgr C in a low emission region in the MeerKAT image, and samples the general background and foreground 1.28 GHz emission in the CMZ and the Galactic disk. Back1 and Back3 are shown in the top panel of Figure 2; Back2 is shown in the bottom panel of Figure 4.

Table 4 presents the spectral index measurements between the 97 GHz (3 mm) ALMA continuum image and the 1.28 GHz MeerKAT image in the regions indicated in Table 1. The columns labeled SB(97) and SB(1.3) give the 97 and 1.38 GHz mean SB in each region in mJy arcsec^{-2} without any background subtraction. The column α_{raw} gives the spectral indices computed from these fluxes. The presence of 1.28 GHz emission throughout the entire CMZ implies that a better estimate of the spectral index for small features localized in the Sgr C H II region requires removal of a background. We used the three regions described above to estimate this background. Columns SB1(1.3), SB2(1.3), and SB3(1.3) are SB estimates of compact regions (in mJy arcsec^{-2} units) after subtracting the mean SB values in regions "Back1," "Back2," and "Back3," respectively. Columns α_1 through α_3 give the corresponding spectral index values between 97 and 1.28 GHz for SB1(1.3) through SB3(1.3).

Table 4 shows that the radio spectral indices of brightest filaments in the JWST Br α image in the Sgr C H II region are dominated by free–free emission. Although no background subtraction, or using backgrounds in regions "Back1" and "Back3," located outside the H II region, yield negative spectral indices indicative of strong nonthermal emission, use of the "Back2" region (which is inside the H II region; Figure 4) for background subtraction to estimate the 1.3 GHz radio flux gives an index close to −0.1, which is expected in the case of optically thin, free–free (i.e., purely thermal) emission (B. T. Draine 2011).

The filaments labeled 1 through 5 form a fragmented, concentric arc of emission wrapping around the Sgr C cloud with a radius of ~45″ (~1.85 pc). Given that, with background subtraction, the spectral indices between 97 and 1.28 GHz are close to flat—slightly negative using the flux in "Back 1" and slightly positive using the mean flux in "Back 2"—it is likely that the numbered features trace ionization fronts dominated by thermal free–free emission with some contribution of emission from warm dust. Although the radio continuum emission

between 97 and 1.28 GHz is dominated by the free–free process, the negative spectral index in the 1 to 2 GHz region (i.e., in the MeerKAT spectral index map; see Figure 2) indicates the presence of some nonthermal component, likely synchrotron radiation. We therefore hypothesize that the unusual filamentary morphology of Sgr C results from confinement of the H II region plasma by strong magnetic fields.

3.6. A Simple Model of Filamentary, Magnetically Dominated H II Regions

The filamentary morphology of the MeerKAT, ALMA, and NIRCam data can be explained by confinement of thermal plasma by strong magnetic fields. We present a simple model for the evolution of H II plasma in highly structured, strong magnetic fields, which can explain the unique appearance of the Sgr C H II region. This picture may explain filamentary structure of the CMZ H II regions in general, and therefore would be applicable to photoionized plasmas in all galactic nuclei.

Magnetic fields play pivotal roles in star formation (P. Hennebelle & S.-I. Inutsuka 2019; K. Pattle & L. Fissel 2019; K. Pattle et al. 2023). However, when massive stars form in the Galactic disk, the thermal pressure of photoionized plasma tends to dominate the evolution of their H II regions. A number of studies have explored the roles of magnetic fields in the formation and evolution of H II regions. M. R. Krumholz et al. (2007) integrated a magnetohydrodynamic (MHD) code into the existing hydrodynamic framework for modeling H II region evolution. J. D. Soler & P. Hennebelle (2017) present models of cloud collapse and evolution in the presence of magnetic fields. J. C. Ibáñez-Mejìa et al. (2022) explore the relationship between field orientations, density gradients, and flows. S. J. Arthur et al. (2011) and M. Zamora-Avilés et al. (2019) found that magnetic fields inhibit H II region expansion perpendicular to the field lines but allow expansion parallel to the field lines. As H II regions grow, this leads to anisotropic development. J. Mackey & A. J. Lim (2011) present MHD simulations of pillar formation at H II region edges under uniform B-fields up to 160 μG. B-fields perpendicular to the pillar axes tend to create ribbons of plasma expanding from the tip of the pillar at right angles. Parallel fields tend to produce ribbons of plasma expanding back into the H II region parallel to the pillar axis. In highly magnetized environments such as the CMZ, these trends will tend to be amplified. These authors suggest that, in highly magnetized H II regions, such filamentary structures would be readily observable in plasma tracers (e.g., recombination lines such as Br α at 4.05 μm).

Most literature on H II region evolution in a magnetized medium considers relatively weak ($\leqslant$50 μG) fields typical of the Galactic disk star-forming regions (see, e.g., C. L. Van Eck et al. 2011). Furthermore, most works assume uniform initial field configurations (M. R. Krumholz et al. 2007; S. J. Arthur et al. 2011; J. Mackey & A. J. Lim 2011; M. Zamora-Avilés et al. 2019). The magnetic fields in the CMZ are orders of magnitude stronger than in the Galactic disk near the Sun, with CMZ field strengths ranging from 100 μG to over 1 mG (K. Ferrière 2009). The hundreds of NTFs indicate that the fields are not uniform. They tend to be confined to ropes or sheets (see, e.g., Figures 1 and 3). Nonetheless, the formation of filaments in strongly magnetized H II regions is suggested in previous literature; as mentioned, J. Mackey & A. J. Lim

(2011) considered H II region evolution in regions with magnetic fields of ~200 μG, finding the formation of filamentary striations in the plasma. It is likely that in even stronger and anisotropic magnetic fields, such as those in the CMZ, the formation of filamentary structure in H II regions would be even more pronounced. The morphology of the Sgr C H II region provides direct observational evidence of this.

We propose that the CMZ H II regions evolve in a highly magnetized medium, and that this environment produces the filaments seen in Sgr C. The plasma β (thermal pressure dominates over magnetic pressure; Equation (4)) is large in Galactic plane H II regions (based on typical Galactic disk field strengths; R. M. Crutcher 2012). On the other hand, the plasma β in the CMZ may be very low (magnetic pressure dominates over thermal pressure), as shown below.

In a high β regime, the expansion of H II regions is driven by thermal pressure (Equation (3)). In a low β environment, the magnetic pressure (Equation (5)) will dominate. Using an electron density of $n_{ii} = 300$ cm^{-3} (J. P. Simpson 2018) and a plasma temperature of $T_{ii} = 6000$ K gives a thermal pressure $P_{ii} \approx 5 \times 10^{-10}$ dynes cm^{-2} for the Sgr C H II region. At this density, the plasma β will be less than 1 for a field stronger than 79 μG. For a 1 mG field, typical of dense CMZ molecular clouds (K. Ferrière 2009; T. Pillai et al. 2015), $P_B \approx 4 \times 10^{-8}$ and $\beta \sim 1.2 \times 10^{-2}$. In the high β (i.e., thermally dominated) limit, H II region evolution will proceed according to the standard Oort–Spitzer description (B. T. Draine 2011), modified by the density structure of the environment and the actual evolution of the stellar Lyman continuum luminosity. As the H II region density and pressure drop (e.g., due to outward expansion) in a highly magnetized medium, β declines and eventually enters the low-β regime, after which the structure of the magnetic field will direct further nebular evolution. In an ideal, uniform density, uniform field environment, the initial, high-β expansion would displace the field, trapping it in a D-type (dense shell) ionization front. As β drops below 1, the H II region would preferentially continue to expand along the field lines without significant growth at right angles to the field.

If a magnetized rope or sheet is loaded with neutral gas below a critical density, n_{crit}, Lyman continuum radiation will drive an R-type (rapid) ionization front through the cloud with a speed faster than twice the sound speed in the plasma. The abrupt increase in temperature will raise the thermal pressure, causing the field and trapped plasma to expand. This critical density of neutral gas (in cm^{-3}) is given by

$$n_{crit} \approx (3Q/(4\pi\alpha_B))^{1/2}R^{-1/2}D^{-1} \qquad (6)$$

where Q is the Lyman continuum luminosity of a star (or group of stars) located at a distance D from a magnetized filament with radius R, or a sheet with half-thickness R, and $\alpha_B \approx 2.6 \times 10^{-13}T_4^{-0.83}$ cm^{-3} s^{-1} is the case-B recombination coefficient for hydrogen with the plasma temperature measured in units of $T_4 = 10^4$ K (B. T. Draine 2011).

If the density in the magnetized region is much greater than n_{crit}, but the surrounding regions have a lower density, the ionization front will race around the dense region, but stall when it hits the dense gas. The increased pressure behind the ionization front will drive a D-type (dense) shock front that jumps out ahead of the ionization front and compresses the medium. As the surface layers of a magnetized filament are ionized, magnetic fields and plasma are peeled off. But, the ram pressure of this magnetized photoablation flow will tend to

compress the colder neutral gas in the rope or sheet, as well as the magnetic field.

This picture differs from the standard description of propagating D-type ionization fronts in several ways. First, soft, nonionizing UV will preheat the neutral medium, weakening the shock that would, in the isothermal limit, compress gas prior to becoming ionized. Second, the magnetic field will also resist compression. The magnetic field pressure may eliminate the D-type shock discontinuity altogether by converting it into a so-called C-type (continuous) structure, in which fluid variables change gradually rather than abruptly. Third, ionized plasma will preferentially flow along the field lines, forming filaments aligned with the field, rather than orthogonal to the ionization fronts as in the standard, nonmagnetized picture of photoablation.

4. Discussion

Among visual and near-infrared emission nebulae, filamentary structure tends to be associated with shock fronts, ionization fronts, and photon-dominated regions (PDRs). Filaments generated by shocks are commonly seen in supernova remnants (SNRs), some stellar wind bubbles, planetary nebulae, various types of outflows from stars, and superbubbles. Examples include the relatively nearby Crab Nebula, Cas A, Veil Nebula, and Simeis 147 SNRs, the NGC 2359 ("Thor's Helmet") stellar wind bubble, protostellar bow shocks such as those in HH 46/47, and the Orion-Eridanus superbubble. The Mittelman, di Cicco, and Walker Hα survey provides one of the deepest, wide-field surveys of the local interstellar matter (ISM) in a hydrogen recombination line.[14] These ultradeep Hα images of the local ISM (within about 1 kpc of the Sun) show extensive, faint filaments, and have led to the discovery of new, but faint, supernovae remnants (R. A. Fesen et al. 2024). Filaments such as those tracing shocks moving at right angles to our LOS are limb brightened because the LOS is nearly tangent to the shock front. When such filaments move into a uniform medium, they can be relatively straight. But, the filaments in the postshock environment tend to present a chaotic jumble of curved structure. The Crab, Veil, and Simeis 147 SNR are good examples. Ionization fronts and PDRs tend to have a softer appearance and are often usually associated with dramatic increases in extinction as one moves from the ionized H II region or soft-UV dominated bubble into the surrounding neutral medium. Ionization fronts and PDRs tend to exhibit highly clumpy structure.

It is possible that some filaments seen in the Sgr C JWST field, especially those that lie beyond the projected outer boundary of the Sgr C H II region, are shock waves similar to those seen in SNRs and stellar wind bubbles near the Sun. Alternatively, the fainter filaments outside the projected edge of the H II region may trace magnetically confined plasma ionized by OB stars outside Sgr C. These filaments may be located anywhere along the LOS through the CMZ. Although some filaments in the projected interior of the Sgr C H II region may also be foreground or background objects, the majority are likely ionized by the Sgr C OB and WR stars. Evidence for this claim is based on the high SB of these features compared to those outside the H II region. However, since there are two WR stars in Sgr C, it is possible that this H II region has been

processed by stellar winds bubbles and possibly by supernovae. The linear morphology of these filaments makes it unlikely that most owe their origins to such shocks. Hence, we propose that magnetized sheets or ropes are a more likely cause of this morphology.

The approximately flat Galactic rotation curve within a few hundred parsecs of the CMZ (M. C. Sormani et al. 2020, 2022) will tend to drive a shear dynamo, resulting in the dominance of the toroidal component of the magnetic field in the dense gas, traced by polarized submillimeter emission of the dust (A. Mangilli et al. 2019). However, the majority of NTFs show that there is a poloidal component to the field (M. Morris 2007). Bubble expansion driven by H II regions, stellar winds, supernovae, and superbubbles may lift field lines and plasma away from the dense gas near the midplane of the Galactic disk, where most of the stellar feedback sources were born. Since, in the midplane, the bubble walls tend to be orthogonal to the Galactic plane, fields swept-up into the bubble walls (appearing as, e.g., NTFs) will also tend to be orthogonal and trace a poloidal field component (Y. Sofue 2023). The "Radio Arc" near l ~0°.18, which is at the high-longitude edge of a compact superbubble, and spatially associated with the massive Arches and Quintuplet clusters (as well as "The Sickle," a curved H II region), is a prominent example of this phenomenon (I. Heywood et al. 2022). Hubble Space Telescope Paschen-α data in the vicinity of this region, presented in H. Dong et al. (2011), also show filaments in CMZ H II regions located between Sgr A* and the Arches and Quintuplet clusters.

The large random motions of CMZ clouds superimposed on their ordered circulation about the GC also tend to tangle magnetic fields. Instabilities in magnetized shells and sheets may further fragment the fields into magnetic filaments and ropes. As such, magnetic structures become loaded with relativistic electrons from discrete sources, such as pulsars, or by in-situ particle acceleration by shocks. The resulting synchrotron emission creates NTFs. The enhanced cosmic-ray fluxes in the CMZ ($\zeta \gtrsim 10^{-15}\,\mathrm{s}^{-1}$; E. Carlson et al. 2016) guarantee that neutral atomic and molecular gas will be strongly coupled to the magnetic fields.

The Sgr C molecular cloud appears in silhouette against the surrounding H II region (Figure 3). The absence of obvious ionization fronts at the edges of the cloud, or projected onto its interior, suggests that the clouds lies in front of the ionized region. Additionally, the observed high-dipole moment molecules such as CS, HNCO, etc. indicate that the mean density of the cloud is $n(H_2) > 10^5\,\mathrm{cm}^{-3}$ (Nguyen-Q-Rieu et al. 1991), especially toward its cometary head, where the most luminous IR sources and massive protostars are located. However, some small amount of Brα emission does leak through the upper part of the cloud, which may trace photoionization of the backside.

As stated in the Introduction, X. Lu et al. (2024) used millimeter-wavelength dust polarization measurements to trace the magnetic field orientation in the Sgr C molecular cloud, finding that the field wraps around the cloud, with the predominant orientation parallel to the cloud surface. Most Brα filaments near the projected edge of the cometary cloud do not follow this orientation. Assuming that the cloud surface is being ionized and photoablated by Lyman continuum radiation, the thermal pressure at the ionization front may be locally higher than the magnetic pressure. In this high-β environment, the plasma flow will tend to be along the local density and

Table 5
Summary of Sgr C H II Properties

Method	Raw SB (MJy sr^{-1})	Corrected SB (erg s^{-1} cm^{-2} arcsec^{-2})	L (pc)	EM (cm^{-6} pc)	n_e (cm^{-3})	$M(M_\odot)$ ($M_\odot$)	Q (s^{-1})	Comments
Br α $A(K_s) = 2$ mag	29.27	1.53×10^{-14}	5.83	1.88×10^5	179	1028	0.64×10^{50}	...
Br α $A(K_s) = 3$ mag	29.27	2.49×10^{-14}	5.83	3.06×10^5	229	1313	1.00×10^{50}	...
1.28 GHz	5.86 Jy	42 μJy as^{-2}	5.83	6.28×10^5	328	1915	2.13×10^{50}	Assume f-f

pressure gradient (e.g., away from the ionization front) roughly at right angles to the front. The plasma may drag along the magnetic field, stretching it along the flow direction. This phenomenon may explain why some of the filaments that appear point away from the cloud (see, e.g., Figure 4).

Figure 4 shows that several bright, parsec-scale filaments point back toward the cometary head of the Sgr C cloud, which contains a cluster of luminous submillimeter cores and forming massive protostars (S. Kendrew et al. 2013; X. Lu et al. 2020, 2021; X. Lu et al. 2022; Paper I). Massive protostars tend to drive the most powerful outflows in forming clusters. It is possible that some of these filaments trace the walls of fossil outflow lobes that emerged from the Sgr C molecular cloud. Alternatively, it is possible that magnetic ropes threaded the core of the protocluster and the surrounding medium prior to ionization. If the lower-density medium surrounding the dense cloud was permeated by filaments or sheets of magnetic field prior to being ionized by massive stars, the plasma would flow along the field lines if the plasma β remains well below 1. Although the parsec-scale filaments that run nearly horizontally in Figure 4 do exhibit "wiggles" over their full extent, the shorter filaments constituting the π-shaped structure in the Br α image (Figure 5) are straight, with length-to-width ratios ranging from 10 to over 100. The lack of bends or entanglement may imply that the magnetic pressure in the filaments must be higher than the ram pressures of various flows that would cause deflections. The tension in the field lines must exceed the amplitudes of these forces. The large length-to-width ratio suggests that the plasma β is below about 0.01. However, the parameters derived for the brightest and presumably densest filaments in Table 2 have plasma β values between 0.3 and 0.6. These values were based on the assumption that the projected width of a filament is equal to its LOS depth. The large length-to-width ratios may indicate that these filaments are mostly sheets seen edge-on. In this case, the assumption that their widths are comparable to their LOS depths overestimates their electron densities and thermal pressures.

Nonthermal emission has been seen in other CMZ H II regions. JVLA observations of the Sgr B2 complex show that the envelopes surrounding the various cluster-forming cores in Sgr B2 exhibit nonthermal spectral indices, especially in the extended, V-shaped region Sgr B2 South, located south of the main Sgr B2 clumps (F. Meng et al. 2019). M. Padovani et al. (2019) present a model of nonthermal emission from cosmic rays accelerated in H II regions.

4.1. Ionizing Sources in Sgr C: Wolf–Rayet Stars and Wind Bubbles

There are two spectroscopically confirmed WR stars in Sgr C, 2MASS J17443734-2927557 and J17444083-2926550 (which we shorten to WCL 3734 and WCL 4083, respectively; J. S. Clark et al. 2021). They are of spectral type "WCLd" ("L"

stands for "Late" on the basis of emission line strengths, and "d" stands for "dust" evident in the spectrum; P. A. Crowther 2007; A. Liermann et al. 2012). In general, WCL stars have ionizing photon emission rates of $Q \approx 10^{49}$ H-ionizing photons per second, meaning that these two stars cannot fully account for the estimated ionizing photon emission rate in the region alone ($Q \approx 6$ to 10×10^{49} H-ionizing photons per second). However, while there are almost certainly additional massive, ionizing stars in the region (F. Nogueras-Lara 2024), their locations are unknown.

WCL 3734 and WCL 4083 have been confirmed to lie within the CMZ by T. Oka et al. (2019) on the basis of detection of strong absorption of H_3^+ in their stellar spectra, both from foreground spiral arms and from warm CMZ gas. WCL 3734 is located in the center of the Sgr C H II region. It is roughly centered between a pair of parallel filaments separated by about $3''.3$ (0.13 pc) that can be traced for at least 1.5 pc in length (Figure 5). We propose that this structure traces a cylinder of magnetized plasma that has been displaced by the pressure of a stellar wind from the WR star.

The WR star J17444083-2926550 (WCL 4083) is located northeast of the Sgr C H II region core. WCL 4083 is sandwiched between a group of parsec-scale filaments extending from the surface of the Sgr C GMC. These filaments reconnect about 1 pc to the upper left of WCL 4083 (toward due North in equatorial coordinates; see Figure 4). They may trace the walls of a parsec-scale cavity created by the winds of this WR star, similar to WCL 3734.

WR stellar winds have typical mass loss rates ranging from 10^{-7} to over 10^{-4} $M_\odot$ yr^{-1} with speeds ranging from 1000 to over 4000 km s^{-1} (P. A. Crowther 2007). The interface between the free-flowing WR star wind and the surrounding H II region contains two shocks. The forward shock, driven by the ram pressure of the wind, sweeps-up H II region plasma into a dense shell. A reverse shock propagates back into the free-flowing wind, which thermalizes the wind kinetic energy and creates an X-ray hot (10^7 to 10^8 K) bubble of shocked stellar wind (J. Castor et al. 1975; R. Weaver et al. 1977). The pressure between the forward and reverse shocks is determined by the ram pressure of the forward shock. These fast shocks may be ideal environments for the acceleration of particles to relativistic speeds. While in an unmagnetized, uniform density medium, stellar winds bubbles are expected to be roughly spherical, in a low-β plasma with a strong, organized magnetic field, and with a magnetic pressure that exceeds the ram pressure of the wind, the field will channel the wind bubble into a cylindrical shape. As an example, consider a wind with a speed of 1500 km s^{-1} and a mass-loss rate of 10^{-6} $M_\odot$ yr^{-1} expected of a WCL star (P. A. Crowther 2007). At a radius of 0.13 pc (the radius of the cavity surrounding WCL 3734), the wind ram pressure would be about 5×10^{-9} dynes cm^{-2}. For any field greater than 0.3 mG, the field would dominate the

evolution of the wind bubble, funneling it into the cylindrical morphology seen in Figure 5.

5. Conclusions

We use JWST Br α and nearby continuum images of the Sgr C H II region to measure its physical parameters. These are summarized in Table 5. The intrinsic Br α luminosity and the derived EM depend sensitively on the assumed extinction and the treatment of foreground and background emission estimated from portions of the JWST image away from the H II region. The measurement of these parameters are limited by the high density of stars and their impact on continuum subtraction. The background subtraction and stellar confusion result in a roughly 10% error in the mean SB and EM of the entire H II region (less than the estimated 20% to 20% error in background-subtracted flux measurements for compact features). If the background-subtracted 1.28 GHz MeerKAT flux from the Sgr C H II region were entirely due to free–free emission, the derived EM, mean electron density, and mass would be larger by a factor of 1.5–1.9. This discrepancy is an indirect indication that a large portion of the MeerKAT emission must be produced by the nonthermal, synchrotron process. This conclusion is consistent with the in-band spectral index around 1.28 GHz and provides indirect evidence for a strong magnetic field.

The CMZ is pervaded by filamentary structure across all length scales, from subparsec scales to $\geqslant 100$ pc. NIRCam observations of Sgr C have shown that the filamentation in CMZ H II regions is not only evident in nonthermal emission but also strongly coupled to free–free emission from thermal plasma. This provides evidence that the evolution of H II regions in highly magnetized, anisotropic fields is distinct from the traditional model in the Galactic disk. This has ramifications not only for our understanding of star formation and the flows of mass and energy across the CMZ of our Galaxy, but in all galactic nuclei and any other analogous environments.

The filamentation observed in Sgr C by JWST, and suggested to be ubiquitous across the CMZ by MeerKAT, reveals a pressing need to incorporate the impact of strong magnetic fields into the current understanding of H II region evolution. It is expected that high-density cores giving birth to massive OB stars may encompass a transition from the high to low β regime. The high accretion rates associated with massive star birth may result in bloated stellar photospheres, which are too cool to emit Lyman continuum radiation. As the accretion rate onto the massive star decreases, its photosphere can shrink, heat, and start to emit Lyman continuum. The environment that becomes ionized is likely to have been preprocessed by protostellar jets and outflows. Such flows may have dragged magnetic fields, elongating them along the flow direction.

The plasma created by the ionization of dense gas at the surfaces of circumstellar disks and the surrounding molecular core and clump may be sufficiently dense so that the total pressure is dominated by thermal pressure and turbulence. Disks, cores, and clumps in massive star-forming regions tend to be warm with $T \sim 100$ to 1000 K. Ionization raises the temperature and thermal pressure by 1 to 2 orders of magnitude. If the thermal and magnetic pressures were in rough equipartition during the warm phase prior to ionization, the plasma β of the freshly ionized medium will initially be large. As the plasma expands due to the suddenly increased pressure and flows into previously generated outflow channels

or is funneled by magnetic fields, there may be a transition to the low-β (i.e., magnetically dominated) regime as the plasma density decreases.

There appear to be at least two distinct populations of filaments in the CMZ: the long-studied large-scale (~tens of parsecs), entirely nonthermal (i.e., invisible in recombination emission) filaments, and the parsec to subparsec-scale filaments that have both a nonthermal (synchrotron) and thermal (free–free) component that are strongly coupled. We assert that the latter of these two populations of filaments are prevalent in all CMZ H II regions, due to the presence of strong, anisotropic magnetic fields and ionizing radiation. Further observations of CMZ H II regions (e.g., Sgr B1), especially in hydrogen recombination lines such as Br α and Paschen α, as well as accurate modeling of H II region evolution in CMZ-like environments, will be necessary to probe more of this population of filaments and to affirm the trend of H II region striation observed in Sgr C.

Appendix
Gallery of Magnified Views of the Sgr C H II Region

We present close-up views of selected regions in the Sgr C H II region. Figure 7 shows the entire JWST field on which the locations of the figures shown in this Appendix are shown. Note that in these figures the tick-marks are tilted because the images
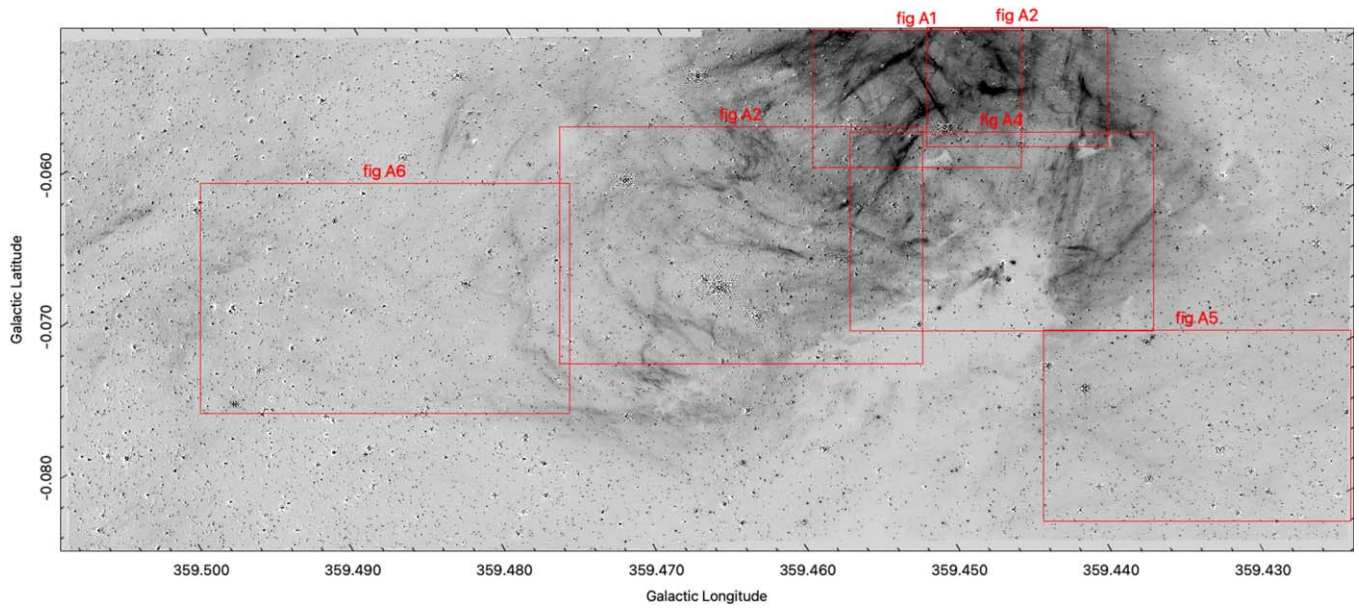
Figure 7. A finder chart showing the locations of the next six figures, labeled from A1 to A6.
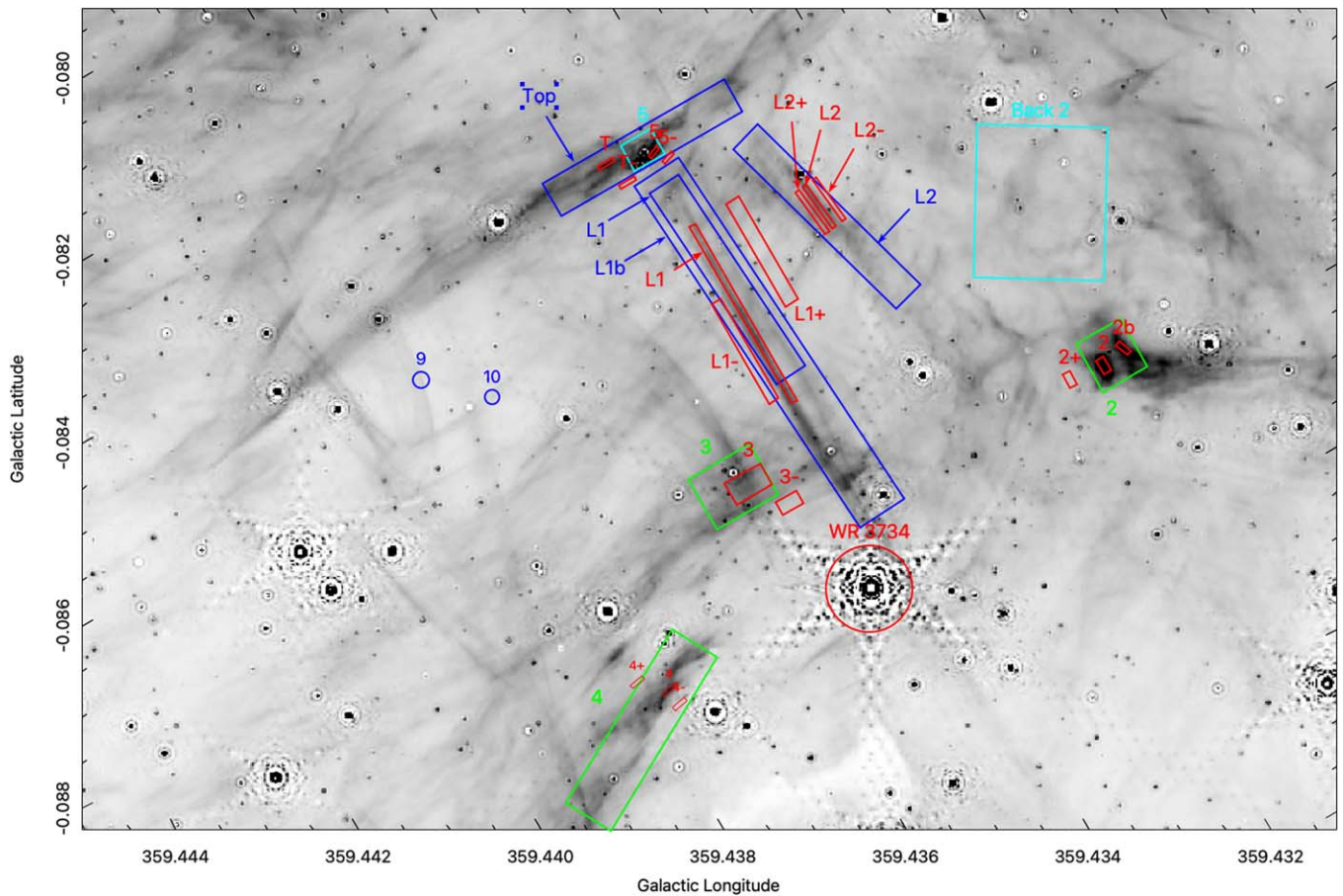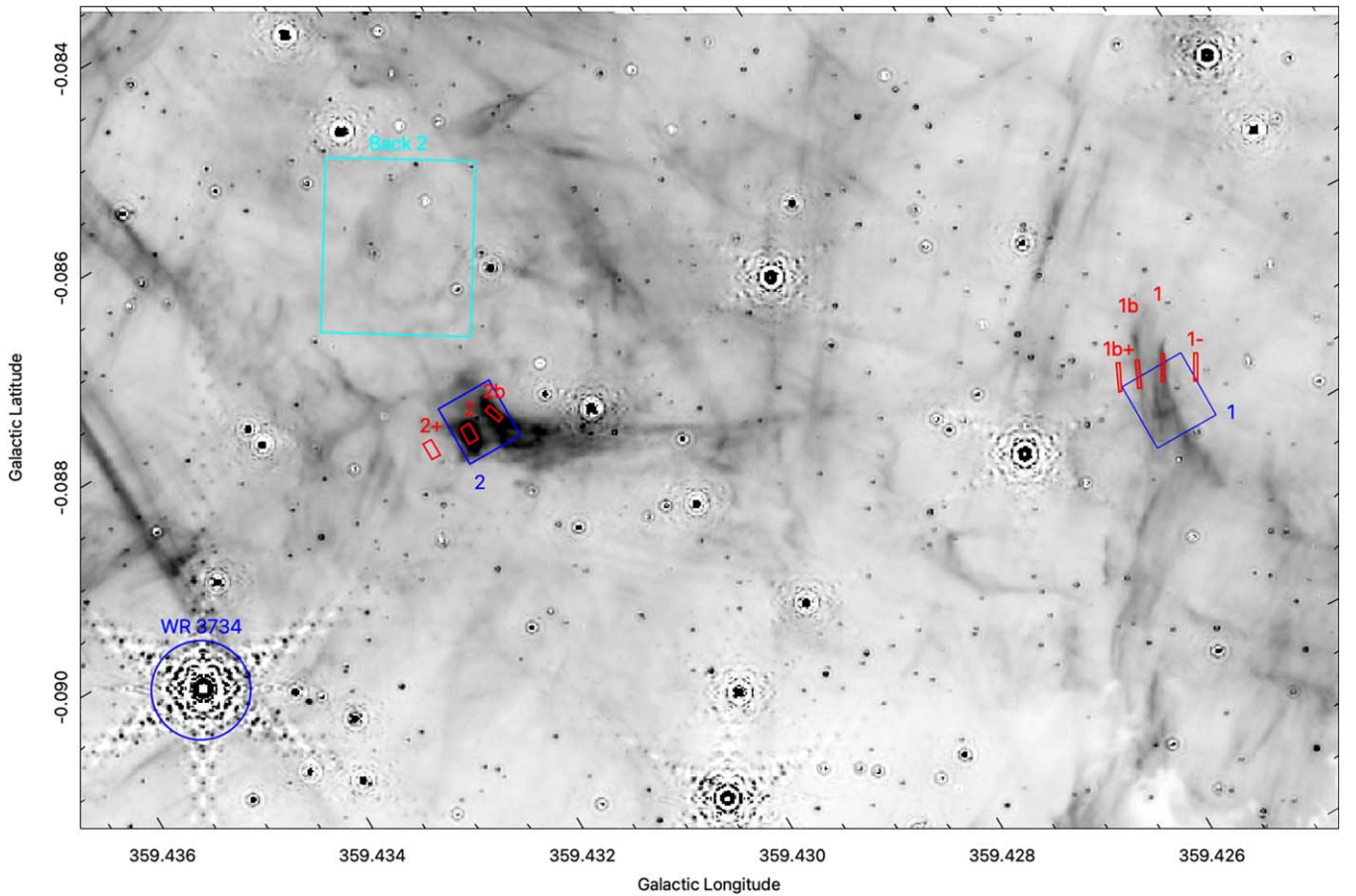

Figure A1. A close-up view of the Br-α emission from the π-shaped filaments, the cylindrical cavity centered on the Wolf–Rayet star WCL 3734, and the inverted V-shaped filaments to the left of the π-shaped filaments. Red boxes show measurement regions used for determining Br α fluxes.

are shown in the JWST pixel coordinate space, which, as shown in Figure 1, is tilted with respect to the Galactic coordinate system.

Figures A1 and A2 show close-up views of the brightest portion of the Sgr C H II region. In Figure A1, note the chain of

V-shaped structures located between Galactic longitudes $359°.440$ and $359°.444$. Close inspection shows these filaments to be double, with two strands separated by a few arcseconds. These figures show the regions used to measure Br α fluxes

Figure A2. A close-up view of the Br-α emission to the right of the π-shaped filaments. Red boxes show measurement regions used for determining Br α fluxes.

(numbered boxes) along with regions used for measuring local backgrounds (numbered boxes with a + and/or − sign). Note the crosshatching pattern of filaments in Figure A2.

Figure A3 shows the Sgr C molecular cloud core, which contains four ultracompact H II regions that are bright and slightly extended in Br α. Note the filaments pointing away from the cloud core. Several of these structures, such as the one pointing roughly toward the right from the high extinction region (2:40 on a clockface) resemble bow shocks and may trace outflow lobes emerging from the opaque cloud to become externally irradiated. The network of stubby, parallel filaments pointing toward 12:30 on a clockface, and located around longitude 359°.435, may also trace outflow lobes. Alternatively, they may trace magnetically confined plasma being photoablated from the molecular cloud. The absence of bright rims or any direct signs of ionization fronts suggests that such fronts are located on the rear side of the cloud and are hidden by many magnitudes of extinction produced by dust in the cloud.

Figure A4 shows bright filaments radiating away from the Sgr C cloud. A pair of wiggly, nearly parallel filaments

separated by about 0°.02 run nearly right to left above the center of this field. While the lower structure disappears around longitude 359°.460, the upper filament bends around toward the bottom to connect with a filament located about 0°.03 below the WR star WR 4083. This morphology resembles a giant bubble blowing out from the cloud surface, located in the lower right corner of the image. It may also be energized by the bright WR star located below and to the left of the image center.

Figure A5 shows the crosshatching pattern of filaments in the lower right of the JWST field. The filament that drops down toward the lower right is suspected to trace an ionization front. The filaments rising toward the right may be magnetically confined structures.

Figure A6 shows details of the left portion of the JWST field beyond what is thought to be the edge of the Sgr C H II region. It is unclear where the excitation for the Br α emission in this portion of the image comes from.

Table 1 lists the measurements regions shown in the figures.
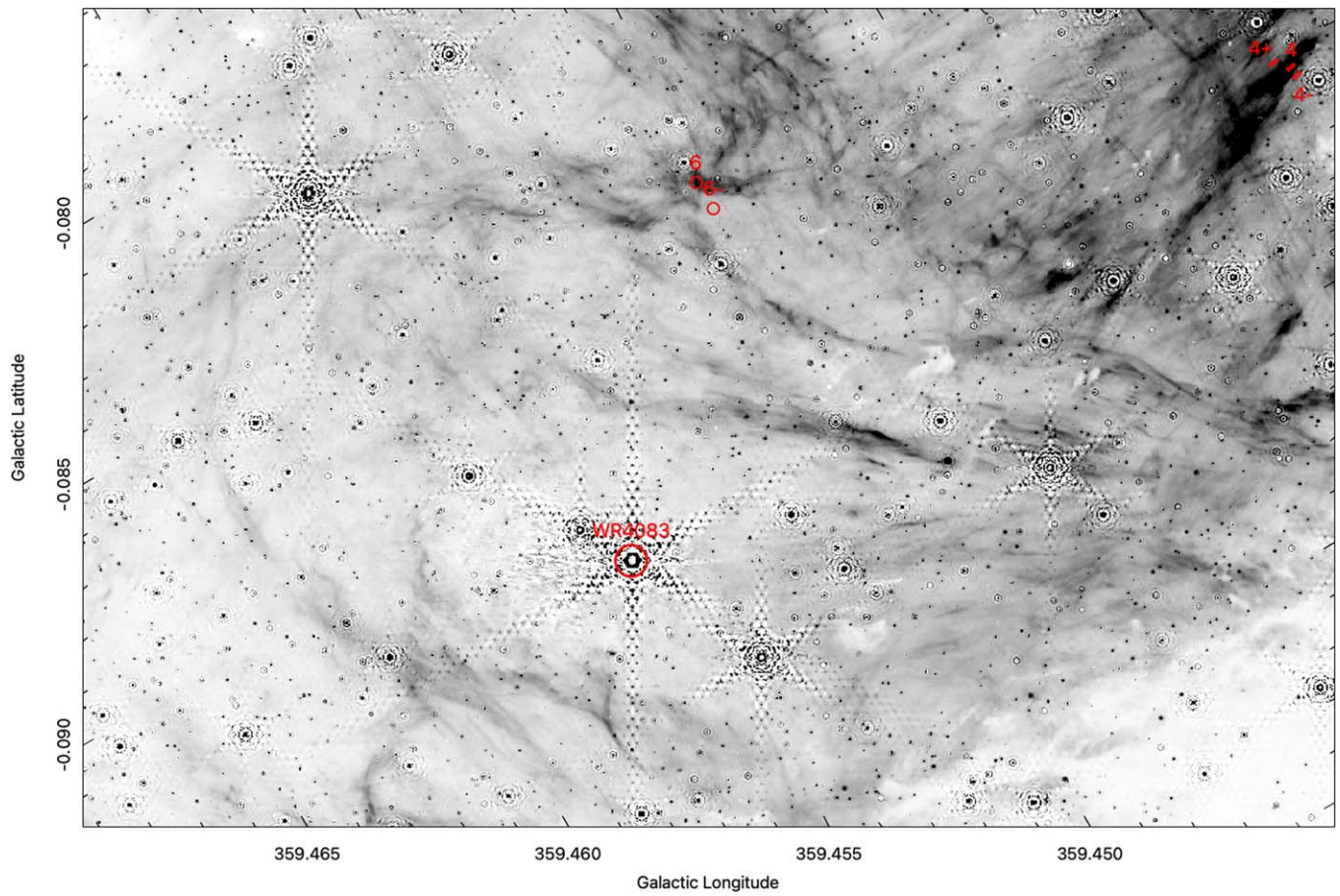
Figure A3. A close-up view of the Br-α emission showing measurement boxes 4 and 6. This field contains radial filaments possibly related to feedback from the Wolf–Rayet star WR 4083.
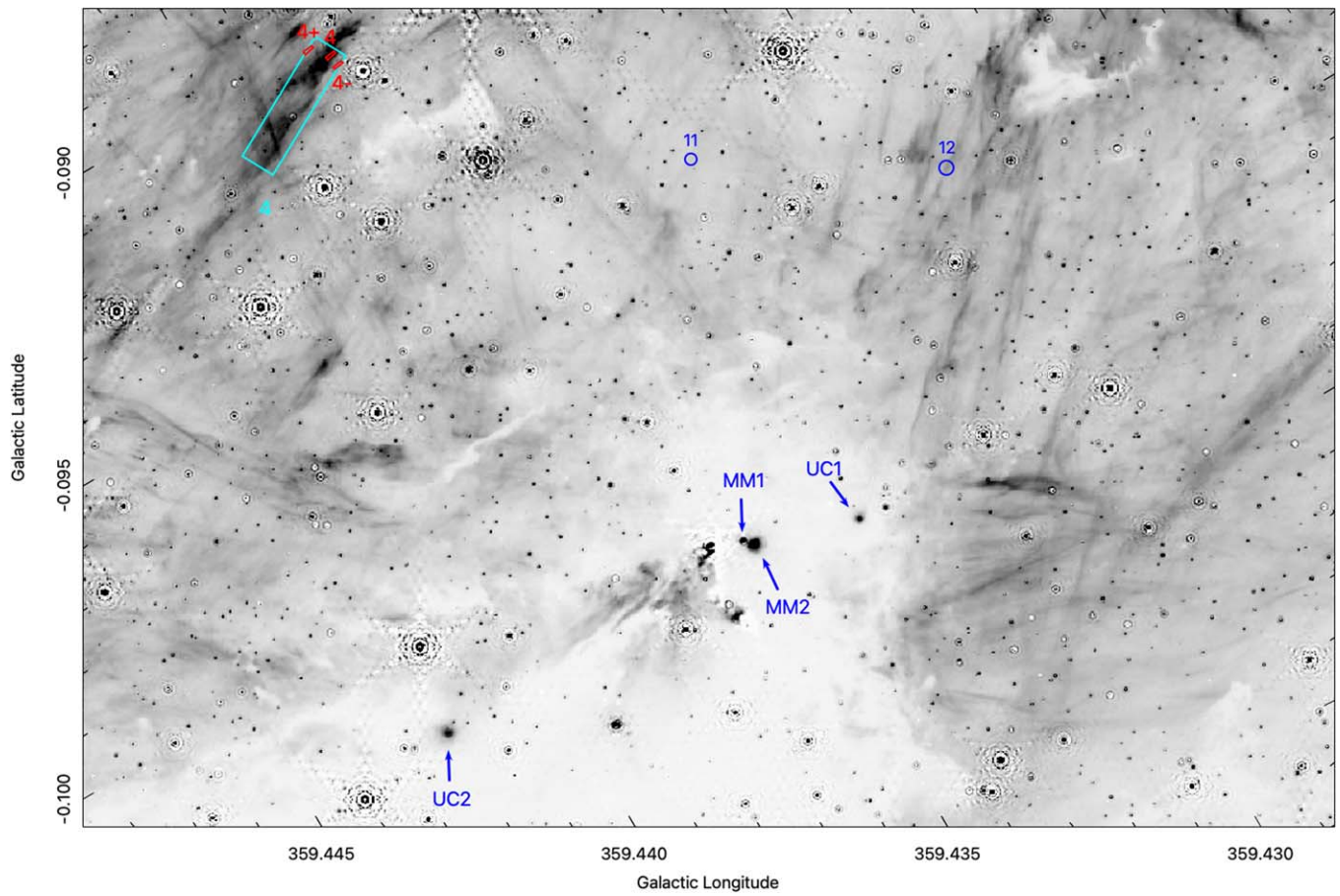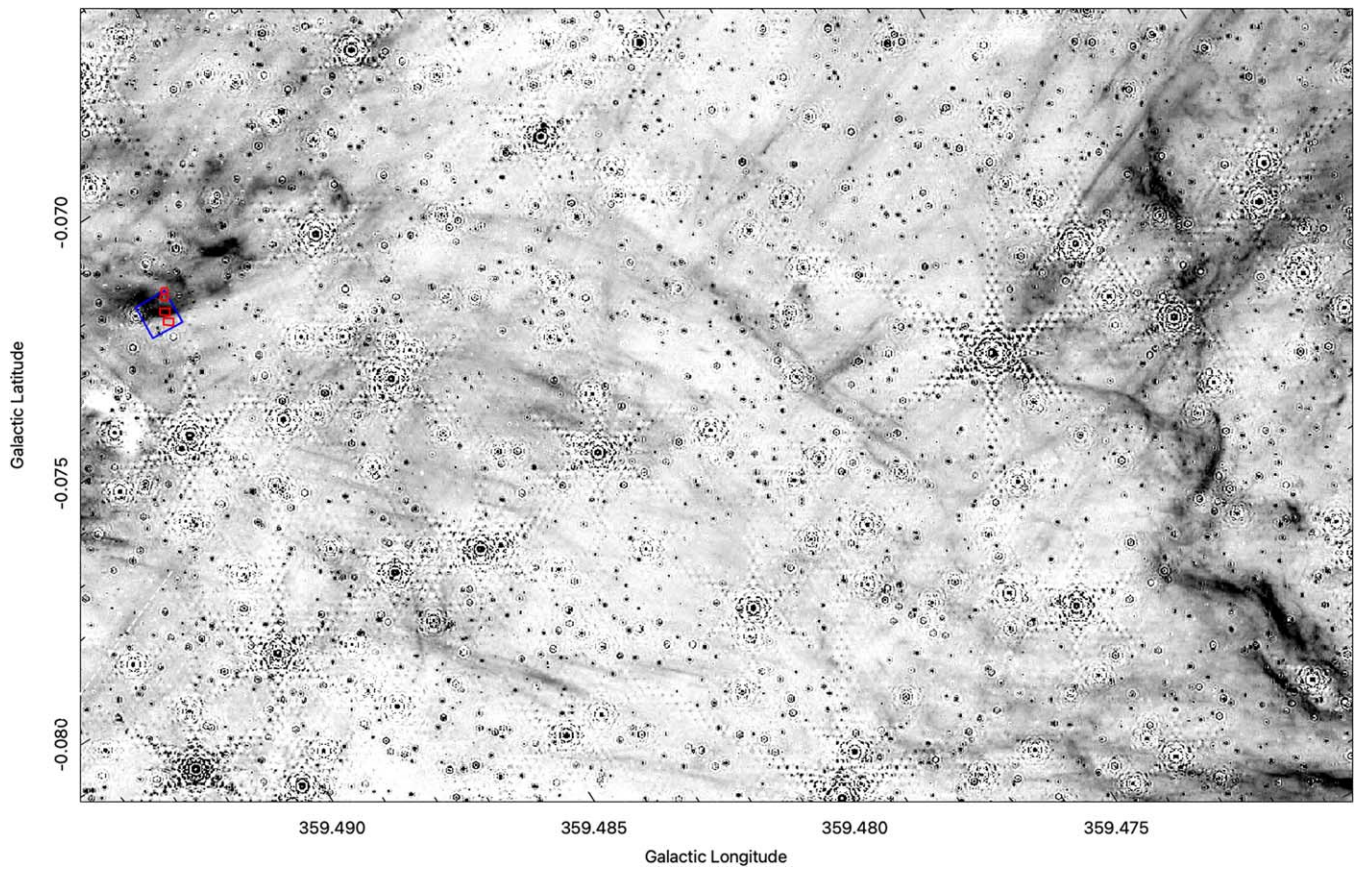
Figure A4. A close-up view of the Br-α emission in the region around the Sgr C molecular cloud core, which hosts several ultracompact H II regions. Measurement box 4 is in the upper left.
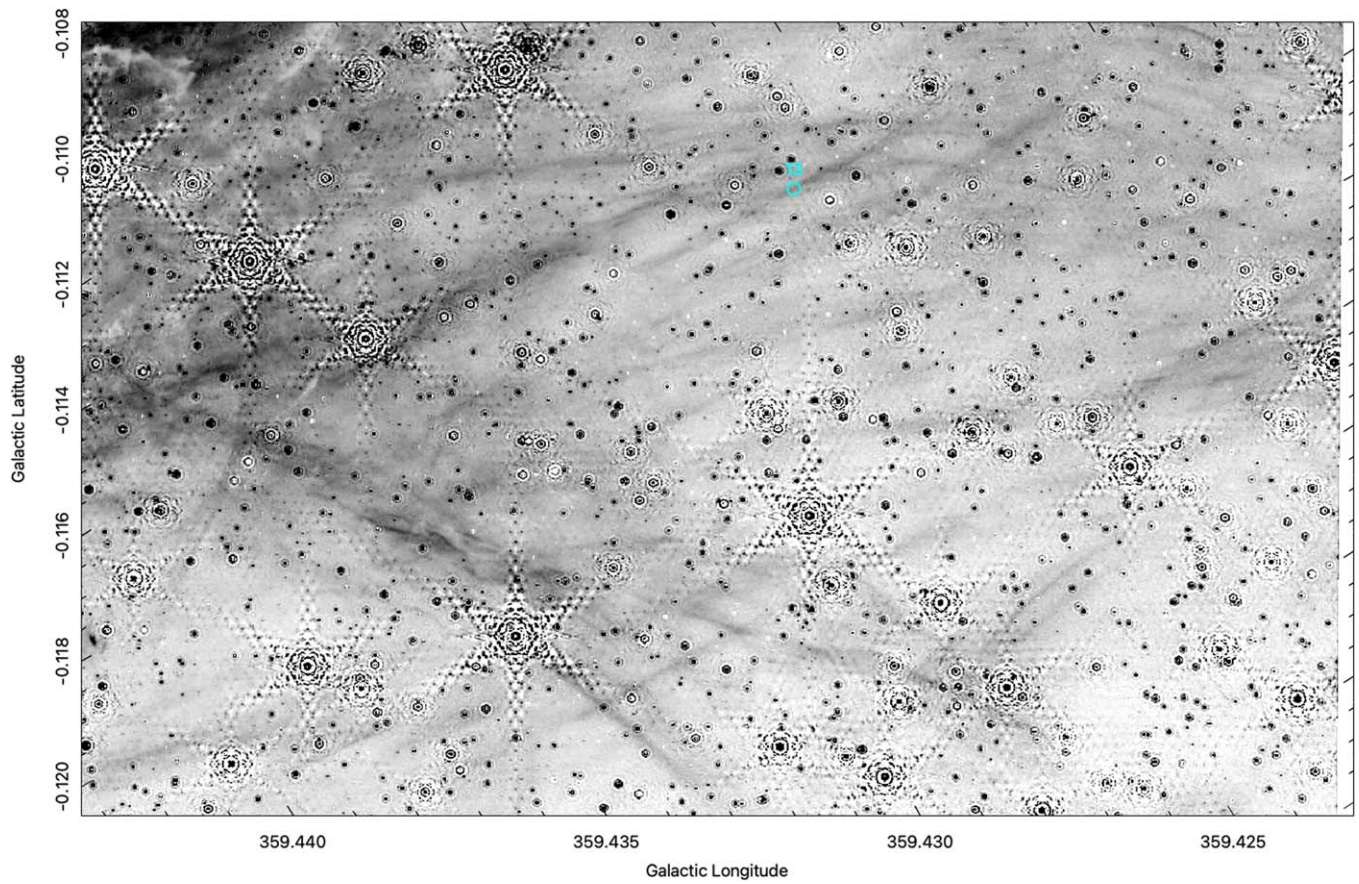
Figure A5. A close-up view of the Br-α emission in the lower right portion of the JWST field.

Figure A6. A close-up view of the Br-α emission in the left portion of the JWST field showing the ionization front at the high-Galactic-longitude edge of the Sgr C H II region (between longitude 359°.470 and 359°.475). It is unclear if the filaments in the left portion of the field are excited by massive stars within Sgr C or other CMZ OB stars. Alternatively, they may trace shocks from supernova remnants in the CMZ.

ORCID iDs

John Bally ⓘ https://orcid.org/0000-0001-8135-6612
Samuel Crowe ⓘ https://orcid.org/0009-0005-0394-3754
Rubén Fedriani ⓘ https://orcid.org/0000-0003-4040-4934
Adam Ginsburg ⓘ https://orcid.org/0000-0001-6431-9633
Rainer Schödel ⓘ https://orcid.org/0000-0001-5404-797X
Morten Andersen ⓘ https://orcid.org/0000-0002-5306-4089
Jonathan C. Tan ⓘ https://orcid.org/0000-0002-3389-9142
Zhi-Yun Li ⓘ https://orcid.org/0000-0002-7402-6487
Francisco Nogueras-Lara ⓘ https://orcid.org/0000-0002-6379-7593
Yu Cheng ⓘ https://orcid.org/0000-0002-8691-4588
Chi-Yan Law ⓘ https://orcid.org/0000-0003-1964-970X
Q. Daniel Wang ⓘ https://orcid.org/0000-0002-9279-4041
Yichen Zhang ⓘ https://orcid.org/0000-0001-7511-0034
Suinan Zhang ⓘ https://orcid.org/0000-0002-8389-6695

References

Arthur, S. J., Henney, W. J., Mellema, G., de Colle, F., & Vázquez-Semadeni, E. 2011, MNRAS, 414, 1747
Bally, J., Stark, A. A., Wilson, R. W., & Henkel, C. 1987, ApJS, 65, 13
Bally, J., Stark, A. A., Wilson, R. W., & Henkel, C. 1988, ApJ, 324, 223
Balser, D. S., Rood, R. T., Bania, T. M., & Anderson, L. D. 2011, ApJ, 738, 27
Biswas, S., Mondal, S., Hoque, A., et al. 2024, ApJ, 961, 176
Butterfield, N. O., Chuss, D. T., Guerra, J. A., et al. 2024a, ApJ, 963, 130
Butterfield, N. O., Guerra, J. A., Chuss, D. T., et al. 2024b, ApJ, 968, 63
Carey, S. J., Noriega-Crespo, A., Mizuno, D. R., et al. 2009, PASP, 121, 76
Carlson, E., Linden, T., & Profumo, S. 2016, PhRvD, 94, 063504
Castor, J., McCray, R., & Weaver, R. 1975, ApJL, 200, L107
Chandrasekhar, S., & Fermi, E. 1953, ApJ, 118, 113
Clark, J. S., Patrick, L. R., Najarro, F., Evans, C. J., & Lohr, M. 2021, A&A, 649, A43
Clark, S. E., Peek, J. E. G., & Putman, M. E. 2014, ApJ, 789, 82
Condon, J. J., & Ransom, S. M. 2016, Essential Radio Astronomy (Princeton, NJ: Princeton Univ. Press)
Crocker, R. M., Jones, D. I., Melia, F., Ott, J., & Protheroe, R. J. 2010, Natur, 463, 65
Crowe, S., Fedriani, R., Tan, J. C., et al. 2025, ApJ, 983, 19
Crowther, P. A. 2007, ARA&A, 45, 177
Crutcher, R. M. 2012, ARA&A, 50, 29
Dong, H., Wang, Q. D., Cotera, A., et al. 2011, MNRAS, 417, 114
Draine, B. T. 2011, Physics of the Interstellar and Intergalactic Medium (Princeton, NJ: Princeton Univ. Press),
Ferrière, K. 2009, A&A, 505, 1183
Ferrière, K., Gillard, W., & Jean, P. 2007, A&A, 467, 611
Fesen, R. A., Drechsler, M., Strottner, X., et al. 2024, ApJS, 272, 36
Fitzpatrick, E. L. 1999, PASP, 111, 63
Fritz, T. K., Gillessen, S., Dodds-Eden, K., et al. 2011, ApJ, 737, 73
Ginsburg, A., Henkel, C., Ao, Y., et al. 2016, A&A, 586, A50
Giveon, U., Sternberg, A., Lutz, D., Feuchtgruber, H., & Pauldrach, A. W. A. 2002, ApJ, 566, 880
Guan, Y., Clark, S. E., Hensley, B. S., et al. 2021, ApJ, 920, 6
Haffner, L. M., Reynolds, R. J., Tufte, S. L., et al. 2003, ApJS, 149, 405
Hankins, M. J., Lau, R. M., Radomski, J. T., et al. 2020, ApJ, 894, 55
Hennebelle, P., & Inutsuka, S.-I. 2019, FrASS, 6, 5
Henshaw, J. D., Barnes, A. T., Battersby, C., et al. 2023, in ASP Conf. Ser. 534, Protostars and Planets VII, ed. S. Inutsuka et al. (San Francisco, CA: ASP), 83
Heywood, I., Rammala, I., Camilo, F., et al. 2022, ApJ, 925, 165
Hu, Y., Lazarian, A., & Wang, Q. D. 2022, MNRAS, 513, 3493
Ibáñez-Mejìa, J. C., Mac Low, M.-M., & Klessen, R. S. 2022, ApJ, 925, 196
Jow, D. L., Hill, R., Scott, D., et al. 2018, MNRAS, 474, 1018
Kendrew, S., Ginsburg, A., Johnston, K., et al. 2013, ApJL, 775, L50

Koch, E. W., & Rosolowsky, E. W. 2015, MNRAS, 452, 3435
Kruijssen, J. M. D., Longmore, S. N., Elmegreen, B. G., et al. 2014, MNRAS, 440, 3370
Krumholz, M. R., Stone, J. M., & Gardiner, T. A. 2007, ApJ, 671, 518
Lang, C. C., Goss, W. M., Cyganowski, C., & Clubb, K. I. 2010, ApJS, 191, 275
Liermann, A., Hamann, W. R., & Oskinova, L. M. 2012, A&A, 540, A14
Liszt, H. S., & Spiker, R. W. 1995, ApJS, 98, 259
Lu, X., Cheng, Y., Ginsburg, A., et al. 2020, ApJL, 894, L14
Lu, X., Li, G.-X., Zhang, Q., & Lin, Y. 2022, NatAs, 6, 837
Lu, X., Li, S., Ginsburg, A., et al. 2021, ApJ, 909, 177
Lu, X., Liu, J., Pillai, T., et al. 2024, ApJ, 962, 39
Lu, X., Mills, E. A. C., Ginsburg, A., et al. 2019, ApJS, 244, 35
Mackey, J., & Lim, A. J. 2011, MNRAS, 412, 2079
Mangilli, A., Aumont, J., Bernard, J. P., et al. 2019, A&A, 630, A74
Meng, F., Sánchez-Monge, Á., Schilke, P., et al. 2019, A&A, 630, A73
Mezger, P. G., & Henderson, A. P. 1967, ApJ, 147, 471
Molinari, S., Bally, J., Noriega-Crespo, A., et al. 2011, ApJL, 735, L33
Morris, M. 2007, arXiv:astro-ph/0701050
Mullens, E., Zucker, C., Murray, C. E., & Smith, R. 2024, ApJ, 966, 127
Nagayama, T., Sato, S., Nishiyama, S., et al. 2009, PASJ, 61, 283
Nguyen-Q-Rieu, , Henkel, C., Jackson, J. M., & Mauersberger, R. 1991, A&A, 241, L33
Nishiyama, S., Hatano, H., Tamura, M., et al. 2010, ApJL, 722, L23
Nishiyama, S., Tamura, M., Hatano, H., et al. 2009, ApJ, 696, 1407
Noguteras-Lara, F. 2024, A&A, 681, L21
O'Dell, C. R. 2001, ARA&A, 39, 99
Oka, T., Geballe, T. R., Goto, M., et al. 2019, ApJ, 883, 54
Padovani, M., Marcowith, A., Sánchez-Monge, Á., Meng, F., & Schilke, P. 2019, A&A, 630, A72
Pan, X., Zhang, Q., Qiu, K., et al. 2024, ApJ, 972, 30
Paré, D., Butterfield, N. O., Chuss, D. T., et al. 2024, ApJ, 969, 150
Pattle, K., & Fissel, L. 2019, FrASS, 6, 15
Pattle, K., Fissel, L., Tahani, M., Liu, T., & Ntormousi, E. 2023, in ASP Conf. Ser. 534, Protostars and Planets VII, ed. S. Inutsuka et al. (San Francisco, CA: ASP), 193
Pattle, K., Ward-Thompson, D., Hasegawa, T., et al. 2018, ApJL, 860, L6
Pillai, T., Kauffmann, J., Tan, J. C., et al. 2015, ApJ, 799, 74
Reid, M. J., Menten, K. M., Brunthaler, A., et al. 2019, ApJ, 885, 131
Simpson, J. P. 2018, ApJ, 857, 59
Sofue, Y. MNRAS 2023, 518, 6273
Soler, J. D., & Hennebelle, P. 2017, A&A, 607, A2
Sormani, M. C., Magorrian, J., Nogueras-Lara, F., et al. 2020, MNRAS, 499, 7
Sormani, M. C., Sanders, J. L., Fritz, T. K., et al. 2022, MNRAS, 512, 1857
Sormani, M. C., Treß, R. G., Ridley, M., et al. 2018, MNRAS, 475, 2383
Tachihara, K., Fukaya, N., Tokuda, K., et al. 2024, ApJ, 968, 131
Tress, R. G., Sormani, M. C., Girichidis, P., et al. 2024, A&A, 2403, 13048
Van Eck, C. L., Brown, J. C., Stil, J. M., et al. 2011, ApJ, 728, 97
Weaver, R., McCray, R., Castor, J., Shapiro, P., & Moore, R. 1977, ApJ, 218, 377
Wink, J. E., Wilson, T. L., & Bieging, J. H. 1983, A&A, 127, 211
Yusef-Zadeh, F. 1990, ApJL, 361, L19
Yusef-Zadeh, F. 2003, ApJ, 598, 325
Yusef-Zadeh, F., Arendt, R. G., & Wardle, M. 2022a, ApJL, 939, L21
Yusef-Zadeh, F., Arendt, R. G., Wardle, M., & Heywood, I. 2023, ApJL, 949, L31
Yusef-Zadeh, F., Arendt, R. G., Wardle, M., Heywood, I., & Cotton, W. 2022b, MNRAS, 517, 294
Yusef-Zadeh, F., Arendt, R. G., Wardle, M., et al. 2022c, MNRAS, 515, 3059
Yusef-Zadeh, F., Arendt, R. G., Wardle, M., et al. 2022d, ApJL, 925, L18
Yusef-Zadeh, F., Hewitt, J. W., Arendt, R. G., et al. 2009, ApJ, 702, 178
Yusef-Zadeh, F., Hewitt, J. W., & Cotton, W. 2004, ApJS, 155, 421
Yusef-Zadeh, F., Morris, M., & Chance, D. 1984, Natur, 310, 557
Yusef-Zadeh, F., Zhao, J.-H., Arendt, R., et al. 2024, MNRAS, 530, 254
Zamora-Avilés, M., Vázquez-Semadeni, E., González, R. F., et al. 2019, MNRAS, 487, 2200
Zhou, J. W., Dib, S., Juvela, M., et al. 2024, A&A, 686, A146